Harvesting singlet and triplet excitation energies in covalent organic frameworks for highly efficient photocatalysis

Ruoyang Liu[1†], Dan Zhao[1,2†], Sailun Ji[3], Haipei Shao[1, 4], Yongzhi Chen[1], Minjun Feng[5], Tie Wang[2,6], Juan Li[7], Ming Lin[4], Tze Chein Sum[5], Ning Yan[6], Shu Seki[3] and Donglin Jiang[1]★

[1]Department of Chemistry, Faculty of Science, National University of Singapore, 3 Science Drive 3, Singapore 117543, Singapore

[2]Joint School of National University of Singapore and Tianjin University, International Campus of Tianjin University, Binhai New City, Fuzhou 350207, China

[3]Department of Molecular Engineering, Kyoto University Katsura, Nishikyo-ku, Kyoto 615-8510, Japan

[4]Institute of Materials Research and Engineering (IMRE), Agency for Science, Technology and Research (A*STAR), 2 Fusionopolis Way, Innovis #08-03, Singapore 138634, Singapore

[5]Division of Physics and Applied Physics, School of Physical and Mathematical Sciences, Nanyang Technological University, 21 Nanyang Link, Singapore 637371, Singapore

[6]Department of Chemical and Biomolecular Engineering, National University of Singapore, 4 Engineering Drive 4, Singapore 117585, Singapore

[7]Institute of Crystalline Materials, Shanxi University, Taiyuan 030006, China

[†]These authors contributed equally to this work.

★Corresponding author. Email: chmjd@nus.edu.sg

Photocatalysis has traditionally been constrained by selective utilization of either singlet or triplet excited states, limiting efficiency and reaction scope. Achieving simultaneous optimization of both states has remained a significant challenge. Here, we introduce donor–acceptor covalent organic frameworks (D–A COFs) that integrate a dual-state activation strategy. The COFs feature segregated columnar π-arrays, aligned micropores, and short donor–acceptor distances. Upon photoexcitation, electron transfer occurs at acceptor units, while energy transfer occurs at donor sites. Additionally, the porous network ensures efficient substrate transport to catalytic centres, while intra- and interlayer hydrogen bonding stabilizes excited states, further enhancing photostability and reactivity. This dual-state strategy sets a new benchmark for photocatalytic organic transformations, including high turnover frequencies under red-light irradiation, broad-spectrum absorption extending into the near-infrared, and operation without metals, co-catalysts, or sacrificial donors. By integrating photophysical and structural optimizations, our approach establishes a new design paradigm, overcoming fundamental limitations in solar-driven chemical transformations and broadening the scope of COF-based photocatalysis.

Main

Photocatalysis is a powerful and versatile tool with far-reaching applications in environmental remediation[1, 2], energy conversion[3, 4], and organic synthesis[5–7]. It not only enables cleaner industrial practices and renewable energy solutions[8], but also unlocks unique reaction pathways with high selectivity and functional group tolerance, facilitating the construction of complex molecular scaffolds that are valuable in pharmaceuticals and fine chemicals[5–7].

In photocatalytic materials, both singlet (S_1) and triplet (T_1) excited states play crucial roles, each offering distinct advantages. The S_1 state, arising from direct photon absorption, is

commonly utilized in photoredox reactions[9]. Despite its relatively short lifetime, it excels in electron transfer processes, enabling thermodynamically challenging redox reactions[10]. Electron transfer also provides precise control over reactant oxidation states[11] and facilitates the generation of highly reactive intermediates to drive organic transformations[10]. This is particularly evident in photocatalytic systems developed for hydrogen evolution, carbon dioxide reduction and hydrogen peroxide generation[12–14]. These systems usually ignore energy transfer processes, as their efficiency is primarily dictated by charge separation and redox potential alignment.

Conversely, the T_1 state, generated via intersystem crossing from S_1, plays a key role in energy transfer processes. With its extended lifetime, T_1 bypasses redox potential constraints[15], enhance photocatalyst stability[16, 17], and can occur over longer distances than electron transfer[18]. These properties have been effectively leveraged in singlet oxygen generation[19], photodynamic therapy (PDT)[20], and Dexter energy transfer (DET) systems[21]. These systems usually focus on energy transfer processes rather than direct electron transfer, relying on the ability of T_1 to facilitate controlled energy migration.

Given these merits, optimizing both excited states are highly desirable for maximizing efficiency, as single-pathway approaches are usually insufficient, especially for photocatalytic organic transformations where both excited states are involved[14]. However, achieving simultaneous optimization has remained a significant challenge. To date, most efforts have focused on optimizing either S_1 for electron transfer[10–14] or T_1 for energy transfer[19–21], rarely both (Fig. 1a). In many instances, studies have relied on the intrinsic properties of COFs[22–24], where electron and energy transfer processes occur passively, dictated by the inherent electronic structure of the material rather than being strategically engineered to maximize efficiency. This has constrained overall photocatalytic performance, as key parameters such as donor–acceptor distance, exciton migration, and charge separation dynamics remain

suboptimal. By employing the S_1 state for electron transfer and the T_1 state for energy transfer, it is feasible to improve reaction efficiencies and extend the range of photoinduced reactions. This dual-state methodology (Fig. 1b) could potentially revolutionize photocatalysis, enabling more efficient solar-to-chemical energy conversions and facilitating complex chemical transformations that are otherwise challenging to achieve.

In this study, we present a dual-state activation strategy that integrates electron transfer and energy transfer in donor-acceptor covalent organic frameworks (D–A COFs), at two different active sites. The COFs effectively harvest both S_1 and T_1 excitation energies to drive various organic transformations with exceptional efficiencies across multiple metrics and expanded applicability to other solar-driven organic transformations.

Results

Structural design and synthesis

We incorporated electron-donating porphyrin and electron-accepting benzothiadiazole units (Fig. 1c) to construct the D–A COFs[25] (Fig. 1d–g). These D–A COFs are distinctive in their ability to harvest both S_1 and T_1 excitation energies to facilitate reactions (Fig. 1h and 1i). Regarding S_1 utilization, upon photoexcitation from the ground state (S_0) to the excited singlet state (S_1), the D–A COFs trigger rapid photoinduced electron transfer and efficient charge separation, generating electrons and holes that are quickly transported to catalytic sites. This establishes an effective charge generation and transport pathway (Fig. 1h). For T_1 utilization, the D–A COFs undergo intersystem crossing from S_1 to T_1 state, enabling the transfer of excitation energy to reactants, thereby enhancing reaction rates and creating a robust excitation energy transfer pathway (Fig. 1h).

The structural design of the D–A COFs contributes to their dual-state functionality through several distinct features. First, the porphyrin unit serves as both an electron donor and

a T_1 state generator, while the benzothiadiazole unit acts as an electron acceptor. Second, the covalently linked porphyrin and benzothiadiazole units arrange biaxially in the 2D plane, at a distance of 1.2 nm (Fig. 1h), forming π stacks at a distance of 4.0 Å in the *z* direction. These segregated D and A columns[26, 27] with proximate intralayer D–A distances and interlayer separations facilitate charge separation, inhibit charge recombination, promote efficient charge transport with minimal reorganization energy (Fig. 1i, yellow and orange arrow), and accelerate T_1 energy migration to enable quick energy transfer to substrates. Third, the ordered 1D micropores allow for timely delivery of substrates to catalytic sites through capillary action[28, 29] (Fig. 1i, silver arrow in pore). Fourth, the D–A COFs efficiently harvest a broad spectrum of light, extending into the near-infrared region, up to 1000 nm, to enhance catalytic activity. Finally, the densely aligned porphyrin and benzothiadiazole units in the D–A COFs serve as multiple oxidation and reduction centres in the electron transfer pathway, while the extensive porphyrin π arrays function as reaction hubs in the energy transfer pathway (Fig. 1i).

We synthesized the D–A COFs, specifically H_2P-BT-COF (Fig. 1d and 1e) and H_2P-BT(OMe)$_2$-COF (Fig. 1f and 1g), through the condensation of porphyrin with benzothiadiazole or dimethoxy benzothiadiazole units, giving yields of 92% and 89%, respectively (Supplementary Fig. 1). Notably, H_2P-BT(OMe)$_2$-COF develops well-defined hydrogen-bonding networks characterised by multipoint, multichain and multidirectional interactions, including interlayer C−H···O and C−H···N hydrogen bonds of 2.17 Å and 2.41 Å (Fig. 1g, inset, dotted purple line) and intralayer C−H···O and C−H···N hydrogen bonds of 2.34 – 2.41 Å (Fig. 1g, inset, dotted pink line), respectively. These interactions are corroborated by the single-crystal structure of its model compound (Supplementary Fig. 2a). The hydrogen bonds restrain vibrational motion, enhancing the generation of the S_1 state[30], while the electron-donating methoxy units raise the frontier orbital energy levels[31], thereby increasing the thermodynamic

driving force for electron transfer. In contrast, these features are absent in H_2P-BT-COF (Fig. 1e, inset) and its model compound (Supplementary Fig. 2b).

Chemical and crystal structures

Powder X-ray diffraction (PXRD) analysis of H_2P-BT-COF revealed major peaks at 3.50°, 4.92°, 6.98° and 22.66°, corresponding to the (100), (110), (200) and (001) facets, respectively (Fig. 2a, blue cross). Owing to steric hindrance, the imine linkage prefers a *cis* C=N configuration, verified by single crystal analysis of the model compound (Supplementary Fig. 3a, Supplementary Table 1). Structural simulation and Pawley refinement[32] (Fig. 2a, red curve) revealed excellent fitting with the AA-stacking mode (Fig. 2a, green curve), yielding unit-cell parameters of a = 2.56 nm, b = 2.57 nm, c = 3.96 Å and $\alpha = \beta = \gamma = 90°$ (Fig. 2b and 2c, Supplementary Table 2, for atomic coordinates see cif file). In contrast, the AB-stacking mode (Fig. 2a, orange curve, Supplementary Fig. 4a) cannot reproduce the experimental peak positions and intensities. H_2P-BT(OMe)$_2$-COF exhibited analogous facets at 3.46°, 4.92°, 7.06° and 22.76°, respectively (Fig. 2d, blue cross). Unlike H_2P-BT-COF, H_2P-BT(OMe)$_2$-COF adopted the typical *trans* C=N configuration of the imine linkage (Supplementary Fig. 3b, Supplementary Table 3). Structural reconstruction followed by Pawley refinement[32] (Fig. 2d, red curve) revealed an excellent fitting with the AA-stacking mode (green curve), producing unit-cell parameters of a = 2.55 nm, b = 2.57 nm, c = 3.91 Å and $\alpha = \beta = \gamma = 90°$ (Fig. 2e and 2f, Supplementary Table 2, for atomic coordinates see cif file), while the AB-stacking mode yielded a poor fit (Fig. 2d, orange curve, Supplementary Fig. 4b). To investigate the preference for *cis* and *trans* configurations in H_2P-BT-COF and H_2P-BT(OMe)$_2$-COF, respectively, we calculated the energies for all possible combination of configurations in both model compounds. The results revealed that the *cis* configuration (Supplementary Fig. 5a and 5b) is energetically favored in BT, whereas the *trans* configuration (Supplementary Fig. 5c and 5d)

is preferred in $BT(OMe)_2$. These align well with our single-crystal analysis, further reinforcing our structural assignments.

Their chemical structures were unambiguously characterised by various analytic methods. Fourier-transform infrared (FT IR) spectroscopy revealed the absence of C=O stretches at 1690 cm^{-1}, with new C=N stretches at 1630 cm^{-1}, indicative of successful imine linkage formation[33] in H_2P-BT-COF (Fig. 2g, orange curve) and H_2P-$BT(OMe)_2$-COF (blue curve). Solid-state ^{13}C cross polarization magic angle spinning nuclear magnetic resonance (CP/MAS NMR) confirmed the presence of carbon atoms from the imine linkage, porphyrin[34] and benzothiadiazole units (Supplementary Fig. 6).

Porous structure and visualization of lattice

Nitrogen sorption isotherm measurements at 77 K (Fig. 2h) revealed type I isotherms, suggesting that H_2P-BT-COF (orange dots and circles) and H_2P-$BT(OMe)_2$-COF (blue dots and circles) are microporous materials[35], hosting Brunauer–Emmett–Teller (BET) surface areas of 1020 $m^2\ g^{-1}$ and 568 $m^2\ g^{-1}$ (Supplementary Fig. 7), pore volumes of 0.44 $cm^3\ g^{-1}$ (Fig. 2i) and 0.31 $cm^3\ g^{-1}$ (Fig. 2j) and micropores of 1.98 nm (Fig. 2i) and 1.73 nm (Fig. 2j), respectively.

Field emission scanning electron microscopy (FE SEM) revealed nanorod crystallites for H_2P-BT-COF (Supplementary Fig. 8a) and H_2P-$BT(OMe)_2$-COF (Supplementary Fig. 8b). High resolution transmission electron microscopy (HR TEM, Fig. 2k-r) unambiguously revealed the highly crystalline structures of COFs, in agreement with the results of XRD and molecular refinement. Low magnification TEM images (Supplementary Fig. 9a and b) displayed rectangular crystal of H_2P-BT-COF with a size of 400 nm × 100 nm, while H_2P-BT(OMe)-COF exhibited an irregular shape of roughly 30 nm × 50 nm. Viewing from (100) zone axis at higher magnification, HR TEM images showed uniform columnar arrangement of

molecular units in both COFs (Fig. 2k and 2o). The corresponding fast Fourier transform (FFT) images (inset of Fig. 2k and 2o) displayed sharp (010) and streaky (001) diffraction spots. The calculated inter-planar spacing from FFT is 2.5 nm for adjacent 010 planes and 0.4 nm for π-π interlayer stacks (Fig. 2l and 2p). The elongated stripes observed at the (001) spots could be attributed to the staking faults in the crystals, in which the benzothiadiazole units could rotate 180 degrees during crystal growth process and result in the formation of two possible configurations in two COF crystals. This flexibility is also reflected in the PXRD where (001) planes show broaden and weak peaks. The inverse FFT (iFFT) images (Fig. 2l and 2p) further revealed the detailed spatial structure. The bright stripes correspond to the COF molecular chains, while the dark stripes in the IFFT images indicate the position of 1D micropores within the COF structure (Fig. 2l-n and 2p-r). The iFFT images coincide with molecular models perfectly, with a 2.5 nm distance between the centres of two adjacent porphyrins in both COFs and a 1.0 nm sized pore of the porphyrin macrocycle (Fig. 2l). In H_2P-BT(OMe)$_2$-COF, the 1.0-nm macrocyclic pore of the porphyrin unit is not observed due to the slightly tilted stacking of the porphyrin predicted in the model structure (Fig. 2p). The HR TEM live profiles (Extended Data Fig. 1) also show a series of sharp, regularly spaced peaks and troughs, reflecting the periodic arrangement of π-columns within the tetragonal COFs.

Thermogravimetric analysis (TGA) confirmed their stability up to 450 °C under nitrogen (Supplementary Fig. 10), while the COFs retained crystallinity even after 48-hour treatment in various solvents (Supplementary Fig. 11).

Optoelectronic properties and energy levels

H_2P-BT-COF (Fig. 3a, orange curve) and H_2P-BT(OMe)$_2$-COF (blue curve) exhibited broad absorption spectra extending into the near-infrared region, up to 1000 nm. Tauc plots revealed that H_2P-BT-COF (Fig. 3b, orange curve) and H_2P-BT(OMe)$_2$-COF (blue curve) possess low

optical bandgap of 1.37 eV and 1.41 eV, respectively. The introduction of electron-donating dimethoxy units in H_2P-BT$(OMe)_2$-COF raise the conduction band from –0.59 V to –0.95 V and the valence band from 0.78 V to 0.46 V (Fig. 3c, orange and blue plots, Supplementary Fig. 12), consistent with projected density of states (PDOS) (Fig. 3d and 3e, Supplementary Fig. 13). Due to the extensive hydrogen-bonding networks, H_2P-BT$(OMe)_2$-COF exhibited suppressed rotation and vibration, elongating its S_1 lifetime to 6.67 ns (Supplementary Fig. 14a and b, blue curves, Supplementary Table 4), longer than that (5.73 ns) of H_2P-BT-COF (Supplementary Fig. 14a and c, orange curves, Supplementary Table 4). Impedance (Fig. 3f) and photocurrent measurements (Fig. 3g) concordantly demonstrated that H_2P-BT$(OMe)_2$-COF (blue curve) surpassed H_2P-BT-COF (orange curve) in charge transfer and generation. H_2P-BT-COF exhibited dispersed highest occupied molecular orbital (HOMO, Fig. 3h) and lowest unoccupied molecular orbital (LUMO, Fig. 3i). In contrast, in H_2P-BT$(OMe)_2$-COF, HOMO (Fig. 3j) is localised at the porphyrin unit while LUMO (Fig. 3k) is confined to the dimethoxy benzothiadiazole unit.

Charge transport and mass supply

H_2P-BT-COF and H_2P-BT$(OMe)_2$-COF develop ordered porphyrin and benzothiadiazole columns across their frameworks. These π columns are expected to provide pathways for charge transport to the catalytic sites, which is a key yet bottleneck process in photocatalysis[36, 37]. Flash-photolysis time-resolved microwave conductivity (FP-TRMC) measurements[38] were performed to reveal inherent charge transporting functions of the D–A COFs upon photoexcitation[39–42]. Interestingly, we observed that H_2P-BT-COF with less interlayer interactions and dispersed frontier orbitals allows hole transporting while H_2P-BT$(OMe)_2$-COF with reinforced interlayer interactions by hydrogen bonds and localised frontier orbitals is ambipolar to transport both hole and electron. H_2P-BT-COF exhibited a photoconductivity ($\Phi\Sigma\mu$) of 2.2×10^{-9} m^2 V^{-1} s^{-1}, which was decreased to 1.8×10^{-9} m^2 V^{-1} s^{-1} in the presence

of SF_6 electron scavenger and was increased to 2.7×10^{-9} m^2 V^{-1} s^{-1} in the presence of Et_3N hole scavenger (Extended Data Fig. 2a), indicating that H_2P-BT-COF is a *p*-type semiconductor. On the other hand, H_2P-BT$(OMe)_2$-COF exhibited a $\Phi\Sigma\mu$ value of 1.3×10^{-9} m^2 V^{-1} s^{-1}, which was decreased to 1.1×10^{-9} m^2 V^{-1} s^{-1} in SF_6 and to 1.3×10^{-9} m^2 V^{-1} s^{-1} in Et_3N (Extended Data Fig. 2b), suggesting that H_2P-BT$(OMe)_2$-COF is ambipolar and transports both hole and electron. From the Et_3N quenching result, the electron mobility was evaluated to be 8×10^{-10} m^2 V^{-1} s^{-1}. To discern the hole transfer value, H_2P-BT$(OMe)_2$-COF was measured in the absence and presence of iodine as an electron scavenger to exhibit a photoconductivity of 2.1×10^{-9} m^2 V^{-1} s^{-1} and 9.3×10^{-10} m^2 V^{-1} s^{-1}, respectively (Extended Data Fig. 2c), leading to a hole mobility of 1.2×10^{-9} m^2 V^{-1} s^{-1}. Thus, H_2P-BT$(OMe)_2$-COF is ambipolar to enable both hole and electron transport with a rather balanced charge carrier mobility (ratio of electron to hole mobility = 0.67).

To further confirm the carrier transport feature of H_2P-BT$(OMe)_2$-COF, we irradiated the sample with 266-nm laser, which increased the photoconductivity to 8.4×10^{-9} m^2 V^{-1} s^{-1} (Extended data Fig. 2d, red curve) owing to the increment of laser power compared to 355 nm-irardiation (Extended data Fig. 2a, black curve). Under ambient conditions and in a saturated O_2 environment, the photoconductivity decreased to 4.2×10^{-9} m^2 V^{-1} s^{-1} (Extended data Fig. 2d, black curve) and 3.4×10^{-9} m^2 V^{-1} s^{-1} (Extended data Fig. 2d, purple curve), respectively. This decline indicates that O_2, acting as an electron scavenger, effectively captures free electrons, thereby interrupting their contribution to photoconductivity. In addition, the photoconductivity was measured under ambient conditions with Net_3, a hole scavenger, and the value decreased slightly to 4.6×10^{-9} m^2 V^{-1} s^{-1} (Extended data Fig. 2d, blue curve). This reduction indicates that NEt_3 quenched holes, thereby diminishing their contribution to photoconductivity. When NEt_3 was introduced under an N_2 atmosphere, the photoconductivity significantly increased to 2.7×10^{-8} m^2 V^{-1} s^{-1} (Extended data Fig. 2d, green curve). The higher

photoconductivity observed under N_2 suggests that NEt_3 suppressed hole recombination, prolonging the lifetime of free electrons and enhancing their mobility. These findings collectively indicate the ambipolar nature of H_2P-BT$(OMe)_2$-COF, where both electrons and holes contribute to photoconductivity, similar to the results conducted at 355 nm.

As photocatalysis using S_1 requires the transport of both hole and electron to their catalytic sites, the ambipolar character of H_2P-BT$(OMe)_2$-COF is highly desired[43]. H_2P-BT$(OMe)_2$-COF develops a unique catalytic scaffold where the porphyrin and benzothiadiazole units serve as oxidation and reduction catalytic sites, while the porphyrin π columns allow hole transport and the benzothiadiazole π arrays enable electron flow, respectively. Such synergistic catalytic and charge transporting functions are highly unified in this D–A COF but rarely achieved in other photocatalytic materials.

On the other hand, mass supply is critical for delivery of reactants and substrates to the catalytic sites, which play an important role in reaction kinetics as well as the use of S_1 and T_1 excitation energies. We observed that H_2P-BT-COF and H_2P-BT$(OMe)_2$-COF facilitate mass transport across the 1D channels via capillary effect, while the presence of polar dimethoxy units on the pore walls endows H_2P-BT$(OMe)_2$-COF with easier mass delivery capability[44]. We selected acetonitrile for its versatility and prevalence as a polar solvent for the photocatalytic reactions[45] and measured acetonitrile adsorption isotherms at 298 K for H_2P-BT-COF (Extended Data Fig. 3a, orange dots and circles) and H_2P-BT$(OMe)_2$-COF (Extended Data Fig. 3a, blue dots and circles). Notably, both COFs trigger capillary effect to exhibit instant and steep acetonitrile uptake at a low P/P_0 of < 0.12, suggesting their high capability of transporting acetonitrile across their 1D nanochannels. Compared to H_2P-BT-COF, H_2P-BT$(OMe)_2$-COF facilitates acetonitrile transport at a lower relative pressure P/P_0. Despite H_2P-BT$(OMe)_2$-COF having only 56% of the BET surface area (568 $cm^3\ g^{-1}$ as compared to 1020 $cm^3\ g^{-1}$), and 70% of the pore volume of H_2P-BT-COF (0.31 $cm^3\ g^{-1}$ as compared to 0.44 cm^3

g^{-1}), it can achieve 90% of acetonitrile uptake as compared to H_2P-BT-COF (250 cm^3 g^{-1} as compared to 277 cm^3 g^{-1}) (Extended Data Fig. 3b). The enhanced transport and higher pore occupancy in H_2P-BT$(OMe)_2$-COF originate from the increased electrostatic charges on the pore surface, attributed to the dense carpet of polar dimethoxy groups (Extended Data Fig. 3c and 3d). Indeed, evaluation of electrostatic potential distribution (Extended Data Fig. 3e and 3f) revealed a greater polarity at the dimethoxy benzothiadiazole unit, which inevitably leads to stronger dipole-dipole interactions with acetonitrile, promoting both adsorption and transport. Adsorption calculations showed that both COFs enable acetonitrile (Extended Data Fig. 3g and 3h) and oxygen (Extended Data Fig. 3j and 3k) adsorption, with access to both porphyrin and benzothiadiazole catalytic sites. Besides, H_2P-BT$(OMe)_2$-COF also showed higher average isosteric heats for both acetonitrile (28.6 kJ mol^{-1}, Extended Data Fig. 3i) and oxygen (8.96 kJ mol^{-1}, Extended Data Fig. 3l), as compared to H_2P-BT-COF (27.4 kJ mol^{-1} for acetonitrile and 8.38 kJ mol^{-1} for oxygen).Therefore, the 1D polar channels of H_2P-BT$(OMe)_2$-COF offer dense highways across the frameworks to supply reactants (organic compounds and O_2) to the catalytic sites timely, promoting photocatalysis kinetics.

Utilisation of S_1 and T_1

Owing to these unique π architectures and porous structures, the D–A COFs harness both S_1 and T_1 to generate intermediates and promote reactions. Upon light irradiation, the D–A COFs are excited to S_1 followed by intersystem crossing to generate T_1, which induces triplet-to-triplet state energy transfer to O_2 and produces singlet oxygen ($^1O_2$). The $^1O_2$ species is highly active to promote condensation and coupling reactions, without the need of any co-catalysts and sacrificial agents. On the other hand, the resultant S_1 triggers photoinduced electron transfer to produce hole and electron in the porphyrin and dimethoxy benzothiadiazole columns, respectively. The dimethoxy benzothiadiazole column induce reduction reaction of O_2 to generate superoxide radical anion ($^{\bullet}O_2^-$) and further promotes the reduction of organic reactants,

while the oxidized porphyrin array triggers the oxidation reaction of organic substrates, thus completing the condensation and coupling reactions, in the absence of co-catalysts and sacrificial reagents. Harnessing reactive oxygen species through efficient cost-effective photocatalysis has a transformative impact across industries and addresses key global challenges, including clean energy production, environmental sustainability, improved healthcare[46–48].

To confirm $^1O_2$ production from T_1, we irradiated the COF samples in aerated acetonitrile with red light of 620 nm in the presence of 2,2,6,6-tetra-methyl-1-piperidine (TEMP) as a $^1O_2$ trap[49]. Electron paramagnetic resonance (EPR) spectroscopy of the H_2P-BT$(OMe)_2$-COF (Fig. 3l, blue curve) and H_2P-BT-COF (orange curve) revealed typical radical signals of 2,2,6,6-tetra-methyl-1-piperidine oxide (TEMPO). Direct evidence of $^1O_2$ generation was obtained through phosphorescence spectroscopy, which revealed a characteristic emission at 1266 nm upon irradiation[50] of H_2P-BT$(OMe)_2$-COF at 620 nm in O_2-saturated acetonitrile (Supplementary Fig. 15).

To investigate the efficiency of photocatalytic $^1O_2$ generation, we irradiated the COF samples at 620 nm in aerated acetonitrile with 1,3-diphenylisobenzofuran[51] as a probe (Fig. 3m). H_2P-BT$(OMe)_2$-COF exhibited a sharp decrease in DPBF absorbance to almost zero within 140 seconds (Supplementary Fig. 16a, Fig. 3m, blue curve), while H_2P-BT-COF showed lesser efficacy (Supplementary Fig. 16b, Fig. 3m, orange curve). Remarkably, compared to various materials reported to date, such as COFs[52–54], conjugated microporous polymers (CMPs) [55, 56] and hybrid photocatalysts[57, 58] (Supplementary Table 5), H_2P-BT$(OMe)_2$-COF demonstrated the highest activity and best performance in $^1O_2$ generation (using DPBF as the probe), featuring (1) low photocatalyst concentration, (2) air as source, (3) long wavelength red light, (4) short reaction time (140 seconds) and (5) high efficiency (> 96%).

To test $^{\bullet}O_2^-$ generation, we irradiated the D–A COFs at 620 nm in aerated acetonitrile with 5,5-dimethyl-1-pyrroline *N*-oxide (DMPO) as a spin trap[59]. EPR spectroscopy revealed the typical signal of DMPO–OH (Fig. 3n) and confirmed the generation of $^{\bullet}O_2^-$, consistent with COF relative conduction band levels as compared to $O_2/^{\bullet}O_2^-$ (–0.35 V, Fig. 3c, dashed black line). This result indicates that 620-nm photoexcitation excites the D–A COFs to S_1, inducing electron transfer from the porphyrin to the dimethoxy benzothiadiazole unit, where the absorbed O_2 is reduced into $^{\bullet}O_2^-$. Femtosecond transient absorption experiments on H_2P-BT(OMe)$_2$-COF revealed complete quenching of the dimethoxy benzothiadiazole anionic radical signal at 420 nm by air due to electron transfer to O_2, while H_2P-BT-COF is less effective (Supplementary Fig. 17). This result is consistent with the fact that electron-donating methoxy groups raises the frontier orbital energy levels, providing greater thermodynamic driving force for $^{\bullet}O_2^-$ generation (Fig. 3c).

Remarkably, H_2P-BT(OMe)$_2$-COF (Fig. 3l and 3n, blue curves) exhibited TEMPO and DMPO–OH signals with a much higher intensities than H_2P-BT-COF (orange curves), suggesting significantly enhanced photocatalytic activities of H_2P-BT(OMe)$_2$-COF in energy transfer to generate $^1O_2$ and electron transfer to produce $^{\bullet}O_2^-$. Adsorption calculations showed similar oxygen loading but a greater average isosteric heat (Extended Data Fig. 1l) for H_2P-BT(OMe)$_2$-COF (0.164 per unit cell, 8.96 kJ mol^{-1}) than H_2P-BT-COF (0.159 per unit cell, 8.38 kJ mol^{-1}), which is another reason for its greater photocatalytic efficiency.

We examined the D–A COFs with red light (620–1000 nm) for condensation and C–C coupling reactions under ambient conditions, including oxidative coupling, condensation reactions and C–C formation reactions through C(sp^3)–H activation/cross-dehydrogenative coupling (CDC) reactions. Photocatalytic oxidative coupling yields pharmaceuticals, polymers and functional materials[60, 61], while photocatalytic condensations are crucial for preparing

various antiviral, antifungal and anticancer drugs[62, 63]. On the other hand, photocatalytic CDC reaction revolutionizes C(sp^3)–H activation and C–C coupling reaction, providing a sustainable atom-economical approach to streamline pathways with minimised synthetic steps and even no byproducts[64, 65]. In these transformations (Supplementary Tables 6 – 8), H_2P-BT(OMe)$_2$-COF features (1) metal-free, sacrificial reagent-free and ambient temperature and pressure conditions, (2) low photocatalyst usage down to 0.45 mol%, (3) utilization of light over a broad wavelength range from visible to lower energy infrared lights, (4) high conversion rate, selectivity and turnover frequency (TOF), (5) broad substrate scope and (6) tolerance of various functional groups (Extended Data Fig. 3).

Photocatalytic oxidative coupling reactions

H_2P-BT(OMe)$_2$-COF functions as a dual-pathway photocatalyst utilising both S_1 and T_1 to facilitate oxidative coupling reactions in aerated acetonitrile at ambient pressure and temperature (Fig. 4a, Supplementary Data 5). As an illustrative example, H_2P-BT(OMe)$_2$-COF converts benzylamine to *N*-benzyl-1-phenylmethanimine (**2a**) within 10 minutes, achieving a conversion of 98%, selectivity exceeding 99% and an exceptional TOF of 1298 h^{-1}. In contrast, H_2P-BT-COF exhibits a 73% conversion after 30 minutes of 620-nm irradiation, with a TOF of 288 h^{-1}, while amorphous H_2P-BT-COF and amorphous H_2P-BT(OMe)$_2$-COF exhibits 22% and 42% conversion, respectively (Supplementary Table 9). Remarkably, H_2P-BT(OMe)$_2$-COF demonstrates an exceptional apparent quantum efficiency (AQE) of 31.6% at 620 nm and maintains robustness over multiple cycles (Supplementary Fig. 18 and 19). In contrast, H_2P-BT-COF displays an AQE of 10.1% under identical conditions. Outstandingly, H_2P-BT(OMe)$_2$-COF maintains its high selectivity (exceeding 99%) and conversion and under infrared light irradiations at 760 nm (2 hours, 99% conversion), 800 nm (1 day, 98% conversion), 940 nm (2 days, 94% conversion) and 1000 nm (4 days, 91% conversion).

Moreover, H_2P-BT$(OMe)_2$-COF achieves its conversion and selectivity exceeding 99% upon 15-min exposure to sunlight.

When comparing reaction efficiency for the same benzylamine substrate, H_2P-BT$(OMe)_2$-COF surpasses the highest TOFs by over four fold, reported for Por-sp^{2}c-COF with TEMPO as a cocatalyst[66] (387 h^{-1}) and exceeds up to four orders of magnitude compared to other state-of-the-art photocatalysts including metal-organic frameworks[67] (MOFs, 125 h^{-1}), CMPs[68] (12.4 h^{-1}), mpg-C_3N_4[69] (0.53 h^{-1}) and WO_3 nanosheets[70] (0.22 h^{-1}), respectively (Supplementary Table 6).

Noteworthily, H_2P-BT$(OMe)_2$-COF displays outstanding activity to a range of substrates (Fig. 4a), tolerating electron-donating methyl (**2b**, **2g** and **2l**), methoxy (**2c**), *tert*-butyl (**2d**) and isopropyl groups (**2h**), as well as electron-withdrawing fluoro (**2e**, **2i** and **2m**), chloro (**2f**, **2j** and **2o**) and bromo (**2k** and **2n**) substituents at *ortho*, *meta* and *para* positions, alongside aromatic heterocycles such as thiophene (**2p**). All these transformations exhibit excellent selectivity (99%), conversion (99%) and rate to complete within 15 minutes.

Photocatalytic condensation reactions

H_2P-BT$(OMe)_2$-COF facilitates the benzimidazole synthesis from *o*-phenylene diamine and aldehydes in O_2-saturated methanol under ambient conditions (Fig. 4b, Supplementary Data 5). The photocatalytic reaction under 620-nm irradiation yields 2-phenylbenzimidazole (**5a**) within 1 hour, achieving 99% conversion, 99% selectivity and a notable TOF of 55 h^{-1}, which is superior to that of H_2P-BT-COF (35 h^{-1}, 71% conversion), while amorphous H_2P-BT-COF and amorphous H_2P-BT$(OMe)_2$-COF exhibits 21% and 22% conversion, respectively (Supplementary Table 10). Remarkably, when comparing efficiency for the same reaction between *o*-phenylene diamine and aldehydes, the TOF of H_2P-BT$(OMe)_2$-COF exceeds other recorded photocatalysts, including BTT-TPA-COF[71] (30 h^{-1}), BTT-CMP-2[72] (26.5 h^{-1}),

MOFs[73] (16.5 h^{-1}), RuPOP[74] (0.49 h^{-1}) and fluorescein[75] (0.02 h^{-1}), by 1.8 to 2750 fold. (Supplementary Table 7).

H_2P-BT$(OMe)_2$-COF promoted reactions of diverse aldehydes with *o*-phenylenediamines. Firstly, electron-donating (Fig. 4b, methyl: **5b**, **5h** and **5n**; methoxy: **5c**, **5i** and **5o**) and withdrawing (fluoro: **5d**, **5j** and **5p**; chloro: **5e**, **5k** and **5q**; bromo: **5f**, **5l** and **5r**; nitro: **5g** and **5m**) substituents at the *ortho*, *meta* and *para* positions of aldehydes yielded products with up to 99% conversion and 99% selectivity within 1 hour. Secondly, multiple-substituted *o*-phenylenediamines (**5s**–**5u**) and aldehydes (**5v**–**5x**) reacted with up to 99% conversion and 99% selectivity. Thirdly, heteroatomic thienyl (**5y** and **5z**) and pyridyl (**5aa** and **5ab**) aldehydes were well-tolerated. H_2P-BT$(OMe)_2$-COF is easy to regenerate by simple filtration, rinse with solvent and dry, while maintaining its activity over multiple cycles without degradation (Supplementary Fig. 20 and 21).

Photocatalytic C–C bond formations via coupling reactions

H_2P-BT$(OMe)_2$-COF promotes the C–C bond formation reactions through the C(sp^3)–H activation of 2-aryl-1,2,3,4-tetrahydroisoquinolines to undergo CDC reactions with various nucleophiles in O_2-saturated methanol, under 620-nm irradiation and ambient conditions (Fig. 4c, Supplementary Data 5). With nitromethane as the nucleophile, H_2P-BT$(OMe)_2$-COF displayed conversions up to 98% and selectivity over 99% with a TOF of 36 h^{-1} (**7a**–**7e**), while H_2P-BT-COF exhibited a 53% conversion in 1.5 hours with a TOF of 17 h^{-1}. On the other hand, amorphous H_2P-BT-COF and amorphous H_2P-BT$(OMe)_2$-COF exhibits 8% and 24% conversion, respectively (Supplementary Table 11). Unexpectedly, when comparing efficiency for the same reaction between nitromethane and 2-phenyl-1,2,3,4-tetrahydroisoquinolines, H_2P-BT$(OMe)_2$-COF surpasses the best photocatalysts reported, such as MOF-6[76] (8.1 h^{-1}),

COF-JLU5[77] (4.9 h^{-1}), Ag/MOF-10[78] (2.0 h^{-1}), TMP-TAPA[79] (0.3 h^{-1}), bismoviologenes[80] (0.003 h^{-1}) and B-COP[81] (0.0002 h^{-1}) by 4.4 to 180000 fold (Supplementary Table 8).

Replacing the nucleophile with dimethyl malonate (**7f**–**7h**), acetone (**7i**–**7m**), malononitrile (**7n**–**7r**), diisopropylphosphite (**7s**–**7x**), or diphenylphosphite (**7y**–**7ab**) maintained the reaction efficiency (Fig. 4c). H_2P-BT$(OMe)_2$-COF catalysed a wide range of substrates, such as electron-donating (methoxy: **7b**, **7p**, **7u**; *tert*-butyl: **7c**, **7k**, **7q**, **7v**, **7aa**; methyl: **7g**, **7j**, **7o**, **7t**, **7z**) and electron-withdrawing 2-aryl substituents (chloro: **7d**, **7l**, **7r**, **7w**; bromo: **7e**, **7h**, **7m**, **7x**, **7ab**). Surprisingly, H_2P-BT$(OMe)_2$-COF activated C(sp^3)–H of 2-aryl-1,2,3,4-tetrahydroisoquinolines with malononitrile to form 2-aryl-1,2,3,4-tetrahydroisoquinoline-1-carbonitrile within 1.5 hours, achieving up to 97% conversion and 99% selectivity (**7n**–**7r**), which bypasses and is much far superior to traditional iridium catalysts with a 90% yield in 10 hours[82]. H_2P-BT$(OMe)_2$-COF is easy to regenerate and robust for multiple cycle use (Supplementary Fig. 22 and 23).

Comparative studies

Comparative studies between H_2P-BT$(OMe)_2$-COF and H_2P-BT-COF clearly revealed that the methoxy groups play key roles in the photocatalysis, owing to the following effects:

(1) Increased thermodynamic driving force for superoxide formation: The electron-donating methoxy groups raise the valence band of the COF (Fig. 3c), thereby increasing the thermodynamic driving force for $\bullet O_2^-$ generation.

(2) Enhanced charge separation and electron transfer efficiency: The methoxy groups reduce the HOMO-LUMO gap, facilitating stronger charge transfer interactions between donor and acceptor units. This leads to a more localised HOMO and LUMO distribution, enhanced photoinduced charge separation (Fig. 3j and 3k), and longer-lived charge-separated states (Fig. 3f and 3g), ultimately improving electron transfer efficiency for $\bullet O_2^-$ formation.

(3) Stabilization of excited states for efficient energy transfer: The methoxy groups introduce intra- and interlayer hydrogen-bonding networks that restrain vibrational motion (Fig. 1g), suppress non-radiative decay, and stabilize S_1 states. This leads to enhanced energy transfer efficiency (Fig. 3m), favouring $^1O_2$ generation.

(4) Transition from hole transport to ambipolar charge transport: Introducing methoxy groups switch from unipolar to ambipolar charge transport (Extended Data Fig. 2), ensuring rapid and long-range electron transport, effectively reducing electron-hole recombination and increasing the number of electrons available for O_2 reduction to $\bullet O_2^-$. Additionally, ambipolar charge transport supports efficient exciton migration, ensuring that triplet excitons reach O_2 molecules without premature relaxation, thereby facilitating $^1O_2$ generation.

(5) Improved solvent uptake and reaction kinetics: The polar methoxy groups enhance the uptake of polar organic solvents (e.g., acetonitrile), promoting efficient O_2 and substrate delivery to active sites. This accelerates photocatalysis kinetics (Extended Data Fig. 3), further supporting both electron and energy transfer pathways.

To exam non-crystalline polymer analogues of these D–A COFs, we synthesized amorphous H_2P-BT-COF analogue and amorphous H_2P-BT(OMe)$_2$-COF analogue (Supplementary Tables 9–11, Supplementary Figures S24 and S25). For photocatalytic benzylamine oxidative coupling reaction, compared to a conversion of 73% and 98% of H_2P-BT-COF and H_2P-BT(OMe)$_2$-COF, amorphous H_2P-BT-COF and H_2P-BT(OMe)$_2$-COF analogues exhibited a conversion of only 22% and 42%, respectively (Supplementary Table 9). For photocatalytic benzimidazole condensation, amorphous H_2P-BT-COF and H_2P-BT(OMe)$_2$-COF analogues displayed a low conversion of 21% and 22%, which is 71% and 99% for H_2P-BT-COF and H_2P-BT(OMe)$_2$-COF, respectively (Supplementary Table 10). For photocatalytic cross-dehydrogenative coupling, the conversion is only 8% and 24% for

457 amorphous H_2P-BT-COF and H_2P-BT(OMe)$_2$-COF analogues, while it is 35% and 98% for
458 H_2P-BT-COF and H_2P-BT(OMe)$_2$-COF, respectively (Supplementary Table 11). The
459 comparative studies confirm that crystallinity of photocatalysts plays an important role in
460 enhancing photocatalytic efficiencies.

461

462 **Photocatalytic sites and mechanistic studies**

463 We conducted a series of control experiments, which revealed that $^1O_2$ (T_1 pathway)
464 and $^{\bullet}O_2^-$ (S_1 pathway) co-existed and played key roles in these reactions (Supplementary Table
465 9 – 11). In situ diffuse reflectance infrared Fourier transform spectroscopy (DRIFTS) of H_2P-
466 BT(OMe)$_2$-COF under O_2 upon irradiation at 620 nm revealed prominent signals attributed to
467 endoperoxide (1205 cm^{-1}), $^{\bullet}O_2^-$ (1177 cm^{-1}) and $^1O_2$ (O–O, 943 cm^{-1}), suggesting the
468 involvement of both T_1 and S_1 pathway intermediates (Fig. 5a)[83].

469 For the electron transfer pathway via S_1, computational studies identified the catalytic
470 site for O_2 activation to be at Site **D** of the dimethoxy benzothiadiazole unit (Fig. 5b, brown
471 line), which hosts the lowest adsorption energy for endoperoxide *OO* formation (–0.89 eV)
472 and the lowest Gibbs energy for subsequent reduction to *OOH intermediate (–2.15 eV) and
473 finally to $^{\bullet}O_2^-$. Concurrently, the holes generated at the porphyrin unit oxidize primary,
474 secondary and tertiary amines to their corresponding cationic radical species, which are
475 subsequently reduced by $^{\bullet}O_2^-$ to yield products, thus completing the catalytic cycle (Fig. 5d,
476 Supplementary Figs. 26 – 28).

477 For the energy transfer pathway via T_1, O_2 adsorption energy on the porphyrin unit was
478 evaluated (Fig. 5c) and we observed that the *β* positions (site **J**, orange line) possess the lowest
479 O_2 adsorption energy (–1.36 eV). Thus, the porphyrin units transfer T_1 energy to $^3O_2$ to produce
480 $^1O_2$. The generated $^1O_2$ then activates benzylamines, *o*-phenylenediamines and isoquinolines

via a cascade of intermediate steps to yield the corresponding products (Supplementary Fig. 26 – 28), thus completing the reaction cycle (Fig. 5d). Notably, despite similar acetonitrile and O_2 average loading per unit cell (Extended Data Fig. 1g and 1h), density distribution analysis revealed greater acetonitrile and oxygen concentrations near the β positions of the porphyrin units in H_2P-BT(OMe)$_2$-COF (Extended Data Fig. 1i and 1l). Hence, H_2P-BT(OMe)$_2$-COF facilitates the supply of substrate and reactant to the catalytic sites and accelerates the reactions.

From these mechanistic results and control experiments, the contribution of S_1 and T_1 to the photocatalysis was evaluated. In the oxidative coupling reaction, the S_1 and T_1 pathways share 38% and 62%, respectively. For the condensation reaction, the S_1 and T_1 pathways contribute 19% and 81%, respectively. In the C–C coupling reaction, the S_1 and T_1 pathways occupy 61% and 39%, respectively. These different contributions are associated with their difference catalytic cycle, energy matching, substrate-photocatalyst interaction and intersystem crossing efficiency (Supplementary Table 9–11).

Conclusions

Addressing the difficulties associated with harnessing both singlet and triplet photo-excitation energies into a cohesive photocatalytic framework represents a major step forward, with potential impacts on renewable energy, environmental remediation and synthetic chemistry. Our research explores this challenge by developing innovative photocatalytic COFs to exploit singlet and triplet states, paving the way for more efficient and versatile photocatalytic systems. This study demonstrates that COFs can be designed to construct well-defined porous donor-acceptor materials, where the ambipolar skeletons can harness concurrently both S_1 and T_1 to develop simultaneously electron and energy transfer pathways, while the segregated ambipolar π arrays transport holes and electrons and the 1D polar pores deliver reactants and substrates timely to the catalytic centres. These unique structural features work together in photocatalysis

and facilitating various condensation and coupling reactions to achieve unprecedent efficiency and selectivity. Remarkably, the photocatalysts exhibit different proportional contributions of S_1 and T_1 to the different reactions, which might be related to the energy levels of reaction intermediates. Our results highlight a general scheme for designing cohesive photocatalysts to utilise both singlet and triplet excitation energies, by merging optimal photoexcited states and frontier energy levels, dense catalytic centres, charge transport pathways and mass supply channels into one material.

References

1. Wang, Q., Gao, Q., Al-Enizi, A. M., Nafady, A. & Ma, S. Recent advances in MOF-based photocatalysis: environmental remediation under visible light. *Inorg. Chem. Front.* **7**, 300–339 (2020).
2. Wang, H. *et al.* A review on heterogeneous photocatalysis for environmental remediation: From semiconductors to modification strategies. *Chin. J. Catal.* **43**, 178–214 (2022).
3. Banerjee, T., Podjaski, F., Kröger, J., Biswal, B. P. & Lotsch, B. V. Polymer photocatalysts for solar-to-chemical energy conversion. *Nat. Rev. Mater.* **6**, 168–190 (2021).
4. He, T. & Zhao, Y. Covalent organic frameworks for energy conversion in photocatalysis. *Angew. Chem., Int. Ed.* **62**, e202303086 (2023).
5. Douglas, J. J., Sevrin, M. J., Stephenson, C. R. J. Visible light photocatalysis: applications and new disconnections in the synthesis of pharmaceutical agents. *Org. Process Res. Dev.* **20**, 1134–1147 (2016).
6. Twilton, J., Le, C., Zhang, P., Shaw, M. H., Evans, R. W., MacMillan, D. W. C. The merger of transition metal and photocatalysis. *Nat. Rev. Chem.* **1**, 0052 (2017).
7. Bellotti, P., Huang, H.-M., Faber, T., Glorius, F. Photocatalytic late-stage C–H functionalization. *Chem. Rev.* **123**, 4237–4352 (2023).

8. Crisenza, G. E. M. & Melchiorre, P. Chemistry glows green with photoredox catalysis. *Nat. Commun.* **11**, 803 (2020).
9. De Kreijger, S., Glaser, F. & Troian-Gautier, L. From photons to reactions: key concepts in photoredox catalysis. *Chem Catal.* **4**, 101110 (2024).
10. Prier, C. K., Rankic, D. A. & MacMillan, D. W. C. Visible light photoredox catalysis with transition metal complexes: Applications in organic synthesis. *Chem. Rev.* **113**, 5322–5363 (2013).
11. Yoon, T. P., Ischay, M. A. & Du, J. Visible light photocatalysis as a greener approach to photochemical synthesis. *Nat. Chem.* **2**, 527–532 (2010).
12. Chen, Y. & Jiang, D. Photocatalysis with covalent organic frameworks. *Acc. Chem. Res.* **57**, 3182–3193 (2024).
13. Mishra, B. *et al.* Covalent organic frameworks for photocatalysis. *Adv. Mater.* **50**, 2413118 (2025).
14. Wang, H. *et al.* Covalent organic framework photocatalysts: structures and applications. *Chem. Soc. Rev.* **49**, 4135–4165 (2020).
15. Sun, K. *et al.* Energy-transfer-enabled photocatalytic transformations of aryl thianthrenium salts. *Nat. Commun.* **15**, 9693 (2024).
16. Strieth-Kalthoff, F. & Glorius, F. Triplet energy transfer photocatalysis: Unlocking the next level. *Chem* **6**, 1888–1903 (2020).
17. Schmitz, M., Bertrams, M.-S., Sell, A. C., Glaser, F. & Kerzig, C. Efficient energy and electron transfer photocatalysis with a coulombic dyad. *J. Am. Chem. Soc.* **146**, 25799–25812 (2024).
18. Closs, G. L. & Miller, J. R. Intramolecular Long-Distance Electron Transfer in Organic Molecules. *Science* **240**, 440–447 (1988).

19. Ghogare, A. A. & Greer, A. Using singlet oxygen to synthesize natural products and drugs. *Chem. Rev.* **116**, 9994–10034 (2016).
20. Singh, N., Sen Gupta, R. & Bose, S. A comprehensive review on singlet oxygen generation in nanomaterials and conjugated polymers for photodynamic therapy in the treatment of cancer. *Nanoscale* **16**, 3243–3268 (2024).
21. Tian, Y. *et al.* Heavy-atom-free covalent organic frameworks for organic room-temperature phosphorescence via Förster and Dexter energy transfer mechanism. *Small Methods* 2401083 (2024).
22. Liu, X. *et al.* Triazine–porphyrin-based hyperconjugated covalent organic framework for high-performance photocatalysis. *J. Am. Chem. Soc.,* **144**, 23396–23404 (2022).
23. Li, P., Dong, X., Zhang, Y., Lang, X. & Wang, C. An azine-linked 2D porphyrinic covalent organic framework for red light photocatalytic oxidative coupling of amines. *Mater. Today Chem.* **25**, 100953 (2022).
24. Wu, C. *et al.* Porphyrin covalent organic framework for photocatalytic synthesis of tetrahydroquinolines. *Chin. Chem. Lett.* **33**, 4559–4562 (2022).
25. Xia, Y., Zhang, W., Yang, S., Wang, L. & Yu, G. Research progress in donor–acceptor type covalent organic frameworks. *Adv. Mater.* **35**, 2301190 (2023).
26. Jin, S. et al. Creation of superheterojunction polymers via direct polycondensation: segregated and bicontinuous donor–acceptor π-columnar arrays in covalent organic frameworks for long-lived charge separation. *J. Am. Chem. Soc.* **137**, 7817–7827 (2015).
27. Jin, S. et al. Charge dynamics in a donor–acceptor covalent organic framework with periodically ordered bicontinuous heterojunctions. *Angew. Chem., Int. Ed.* **52**, 2017–2021 (2013).
28. Chen, Y. *et al.* Hierarchical assembly of donor–acceptor covalent organic frameworks for photosynthesis of hydrogen peroxide from water and air. *Nat. Synth.* **3**, 998–1010 (2024).

29. Zhao, S. *et al.* Hydrophilicity gradient in covalent organic frameworks for membrane distillation. *Nat. Mater.* **20**, 1551–1558 (2021).
30. Fresch, E. & Collini, E. The role of h-bonds in the excited-state properties of multichromophoric systems: Static and dynamic aspects. *Molecules* **28**, 3553 (2023).
31. Li, Y. Molecular design of photovoltaic materials for polymer solar cells: Toward suitable electronic energy levels and broad absorption. *Acc. Chem. Res.* **45**, 723–733 (2012).
32. Pawley, G. S. Unit-cell refinement from powder diffraction scans. *J. Appl. Crystallogr.* **14**, 357–361 (1981).
33. Uribe-Romo, F. J. *et al.* A Crystalline imine-linked 3-d porous covalent organic framework. *J. Am. Chem. Soc.* **131**, 4570–4571 (2009).
34. Shinde, D. B., Kandambeth, S., Pachfule, P., Kumar, R. R. & Banerjee, R. Bifunctional covalent organic frameworks with two dimensional organocatalytic micropores. *Chem. Commun.* **51**, 310–313 (2015).
35. Thommes, M. *et al.* Physisorption of gases, with special reference to the evaluation of surface area and pore size distribution (IUPAC Technical Report). *Pure Appl. Chem.* **87**, 1051–1069 (2015).
36. Zhou, T. *et al.* PEG-stabilized coaxial stacking of two-dimensional covalent organic frameworks for enhanced photocatalytic hydrogen evolution. *Nat. Commun.* **12**, 3934, (2021).
37. Chen, R. *et al.* Rational design of isostructural 2D porphyrin-based covalent organic frameworks for tunable photocatalytic hydrogen evolution. *Nat. Commun.* **12**, 1354 (2021).
38. Blätte, D., Ortmann, F. & Bein, T. Photons, Excitons, and Electrons in Covalent Organic Frameworks. *J. Am. Chem. Soc.* **146**, 32161–32205 (2024).
39. Ghosh, S. *et al.* Identification of prime factors to maximize the photocatalytic hydrogen evolution of covalent organic frameworks. *J. Am. Chem. Soc.* **142**, 9752–9762 (2020).

40. Gordo-Lozano, M. *et al.* Boosting photoconductivity by increasing the structural complexity of multivariate covalent organic frameworks. *Small* **21**, 2406211 (2025).
41. Chen, L. *et al.* The non-covalent assembly of benzene-bridged metallosalphen dimers: photoconductive tapes with large carrier mobility and spatially distinctive conduction anisotropy. *Chem. Commun.*, 3119–3121 (2009).
42. Tajima, K. *et al.* Synthesis and electron-transporting properties of phenazine bisimides. *J. Mater. Chem. C* **13**, 655–662 (2025).
43. Feng, X. *et al.* An Ambipolar conducting covalent organic framework with self-sorted and periodic electron donor-acceptor ordering. *Adv. Mater.* **24**, 3026–3031 (2012).
44. Luo, Z. *et al.* Manipulating p-π resonance through methoxy group engineering in covalent organic frameworks for an efficient photocatalytic hydrogen evolution. *Angew. Chem., Int. Ed.* **64**, e202420217 (2025).
45. Xiong, L. & Tang, J. Strategies and challenges on selectivity of photocatalytic oxidation of organic substances. *Adv. Energy Mater.* **11**, 2003216 (2021).
46. Wen, Y., Yan, J., Yang, B., Zhuang, Z., Yu, Y. Reactive oxygen species on transition metal-based catalysts for sustainable environmental applications. *J. Mater. Chem. A* **10**, 19184–19210 (2022).
47. Zhou, Z., Song, J., Nie, L., Chen, X. Reactive oxygen species generating systems meeting challenges of photodynamic cancer therapy. *Chem. Soc. Rev.* **45**, 6597–6626 (2016).
48. Yang, B., Chen, Y., Shi, J. Reactive oxygen species (ROS)-based nanomedicine. *Chem. Rev.* **119**, 4881–4985 (2019).
49. Shinkarenko, N. V. & Aleskovskii, V. B. Singlet oxygen: Methods of preparation and detection. *Russ. Chem. Rev.* **50**, 220 (1981).

50. Partanen, S. B., Erickson, P. R., Latch, D. E., Moor, K. J. & McNeill, K. Dissolved organic matter singlet oxygen quantum yields: Evaluation using time-resolved singlet oxygen phosphorescence. *Environ. Sci. Technol.* **54**, 3316–3324 (2020).

51. Entradas, T., Waldron, S. & Volk, M. The detection sensitivity of commonly used singlet oxygen probes in aqueous environments. *J. Photochem. Photobiol. B.* **204**, 111787 (2020).

52. Nagai, A. *et al.* A Squaraine-linked mesoporous covalent organic framework. *Angew. Chem. Int. Ed.* **52**, 3770–3774 (2013).

53. Sun, N. *et al.* Photoresponsive covalent organic frameworks with diarylethene switch for tunable singlet oxygen generation. *Chem. Mater.* **34**, 1956–1964 (2022).

54. Feng, X. *et al.* Two-dimensional artificial light-harvesting antennae with predesigned high-order structure and robust photosensitising activity. *Sci. Rep.* **6**, 32944 (2016).

55. Park, K. C., Cho, J. & Lee, C. Y. Porphyrin and pyrene-based conjugated microporous polymer for efficient sequestration of CO_2 and iodine and photosensitization for singlet oxygen generation. *RSC Adv.* **6**, 75478–75481 (2016).

56. Peng, Y.-Z. *et al.* Charge transfer from donor to acceptor in conjugated microporous polymer for enhanced photosensitization. *Angew. Chem. Int. Ed.* **60**, 22062–22069 (2021).

57. Zhang, W. *et al.* Combining ruthenium(II) complexes with metal–organic frameworks to realize effective two-photon absorption for singlet oxygen generation. *ACS Appl. Mater. Interfaces* **8**, 21465–21471 (2016).

58. Xue, F. *et al.* Iridium complex loaded polypyrrole nanoparticles for NIR laser induced photothermal effect and generation of singlet oxygen. *RSC Adv.* **6**, 15509–15512 (2016).

59. Finkelstein, E., Rosen, G. M. & Rauckman, E. J. Spin trapping of superoxide and hydroxyl radical: Practical aspects. *Arch. Biochem. Biophys.* **200**, 1–16 (1980).

60. Choudhury, L. H., Parvin, T. Recent advances in the chemistry of imine-based multicomponent reactions (MCRs). *Tetrahedron* **67**, 8213–8228 (2011).

61. Kobayashi, S., Ishitani, H. Catalytic enantioselective addition to imines. *Chem. Rev.* **99**, 1069–1094 (1999).

62. Salahuddin, M., Shaharyar, M., Mazumder, A. Benzimidazoles: A biologically active compound. *Arab. J. Chem.* **10**, S157–S173 (2017).

63. Gaba, M., Singh, S., Mohan, C. Benzimidazole: An emerging scaffold for analgesic and anti-inflammatory agents. *Eur. J. Med. Chem.* **76**, 494–505 (2014).

64. Bagdi, A. K. *et al.* Visible light promoted cross-dehydrogenative coupling: a decade update. *Green Chem.* **22**, 6632–6681 (2020).

65. Tian, T., Li, Z., Li, C.-J. Cross-dehydrogenative coupling: a sustainable reaction for C–C bond formations. *Green Chem.* **23**, 6789–6862 (2021).

66. Shi, J.-L. *et al.* 2D sp^2 carbon-conjugated porphyrin covalent organic framework for cooperative photocatalysis with TEMPO. *Angew. Chem., Int. Ed.* **59**, 9088–9093 (2020).

67. Johnson, J. *et al.* Porphyrin-metalation-mediated tuning of photoredox catalytic properties in metal–organic frameworks. *ACS Catal.* **5**, 5283–5291 (2015).

68. Battula, V. R. *et al.* Natural sunlight driven oxidative homocoupling of amines by a truxene-based conjugated microporous polymer. *ACS Catal.* **8**, 6751–6759 (2018).

69. Su, F. *et al.* Aerobic oxidative coupling of amines by carbon nitride photocatalysis with visible light. *Angew. Chem., Int. Ed.* **50**, 657–660 (2011).

70. Zhang, N. *et al.* Oxide defect engineering enables to couple solar energy into oxygen activation. *J. Am. Chem. Soc.* **138**, 8928–8935 (2016).

71. Luo, B. *et al.* Benzotrithiophene and triphenylamine based covalent organic frameworks as heterogeneous photocatalysts for benzimidazole synthesis. *J. Catal.* **402**, 52–60 (2021).

72. Han, S. *et al.* Bandgap engineering in benzotrithiophene-based conjugated microporous polymers: a strategy for screening metal-free heterogeneous photocatalysts. *J. Mater. Chem. A* **9**, 3333–3340 (2021).

73. Razavi, S. *et al.* Redox metal–organic framework for photocatalytic organic transformation: the role of tetrazine function in radical-anion pathway. *Inorg. Chem.* **61**, 19134–19143 (2022).

74. Wang, C., Han, Y., Nie, K. & Li, Y. Porous organic frameworks with mesopores and $[Ru(bpy)_3]^{2+}$ ligand built-in as a highly efficient visible-light heterogeneous photocatalyst. *Mater. Chem. Front.* **3**, 1909–1917 (2019).

75. Li, Z. *et al.* Visible-light-induced condensation cyclization to synthesize benzimidazoles using fluorescein as a photocatalyst. *Green Chem.* **21**, 3602–3605 (2019).

76. Wang, C., Xie, Z., deKrafft, K. & Lin, W. Doping metal–organic frameworks for water oxidation, carbon dioxide reduction and organic photocatalysis. *J. Am. Chem. Soc.* **133**, 13445–13454 (2011).

77. Zhi, Y. *et al.* Covalent organic frameworks as metal-free heterogeneous photocatalysts for organic transformations. *J. Mater. Chem. A* **5**, 22933–22938 (2017).

78. Che, Y. *et al.* Ultrasmall Ag nanoparticles on photoactive metal-organic framework boosting aerobic cross-dehydrogenative coupling under visible light. *Appl. Surf. Sci.* **634**, 157699 (2023).

79. Sharma, N., Chauhan, D., Saini, N. & Kailasam, K. Metal-free triazine-based polymeric network for solar-to-chemical conversion: an insight into the aza-henry reaction. *ACS Appl. Polym. Mater.* **5**, 4333–4341 (2023).

80. Ma, W. *et al.* Phosphorescent bismoviologens for electrophosphorochromism and visible light-induced cross-dehydrogenative coupling. *J. Am. Chem. Soc.* **143**, 1590–1597 (2021).

81. Liu, W. *et al.* Difluoroborate-based conjugated organic polymer: A high-performance heterogeneous photocatalyst for oxidative coupling reactions. *J. Mater. Sci.* **54**, 1205–1212 (2019).

82. Wang, H., Lu, W., Sun, Z., Wang, A., Zhou, W., He, M., Chen, Q. α-Cyanation of aromatic tertiary amines using malononitrile as a low-toxic cyanide source under the catalysis of NiGa layered double oxide. *Asian J. Org. Chem.* **9**, 1769–1773 (2020).
83. Liu, R. et al. Linkage-engineered donor–acceptor covalent organic frameworks for optimal photosynthesis of hydrogen peroxide from water and air. *Nat. Catal.* **7**, 195–206 (2024).
84. Thompson, P., Cox, D. E. & Hastings, J. B. Rietveld refinement of Debye–Scherrer synchrotron X-ray data from Al_2O_3. *J. Appl. Crystallogr.* **20**, 79–83 (1987).
85. Bérar, J. F. & Baldinozzi, G. Modeling of line-shape asymmetry in powder diffraction. *J. Appl. Crystallogr.* **26**, 128–129 (1993).
86. Elstner, M. *et al.* Self-consistent-charge density-functional tight-binding method for simulations of complex materials properties. *Phys. Rev. B* **58**, 7260–7268 (1998).
87. Aradi, B., Hourahine, B. & Frauenheim, T. DFTB+, a Sparse Matrix-Based Implementation of the DFTB Method. *J. Phys. Chem. A* **111**, 5678–5684 (2007).
88. Hourahine, B. *et al.* DFTB+, a software package for efficient approximate density functional theory based atomistic simulations. *J. Chem. Phys.* **152**, 124101 (2020).
89. Perdew, J. P., Burke, K. & Ernzerhof, M. Generalized Gradient Approximation Made Simple. *Phys. Rev. Lett.* **77**, 3865–3868 (1996).
90. Steiner, T. The Hydrogen Bond in the Solid State. *Angew. Chem. Int. Ed.* **41**, 48–76 (2002).
91. Qin, C. *et al.* Dual donor-acceptor covalent organic frameworks for hydrogen peroxide photosynthesis. *Nat. Commun.* **14**, 5238 (2023).
92. Luo, Y. *et al.* Sulfone-modified covalent organic frameworks enabling efficient photocatalytic hydrogen peroxide generation via one-step two-electron O_2 reduction. *Angew. Chem., Int. Ed.* **62**, e202305355 (2023).

93. Wang, H. *et al.* A crystalline partially fluorinated triazine covalent organic framework for efficient photosynthesis of hydrogen peroxide. *Angew. Chem., Int. Ed.* **61**, e202202328 (2022).

94. Delley, B. An all-electron numerical method for solving the local density functional for polyatomic molecules. *J. Chem. Phys.* **92**, 508–517 (1990).

95. Akkermans, R. L. C., Spenley, N. A. & Robertson, S. H. Monte Carlo methods in Materials Studio. *Mol. Simul.* **39**, 1153–1164 (2013).

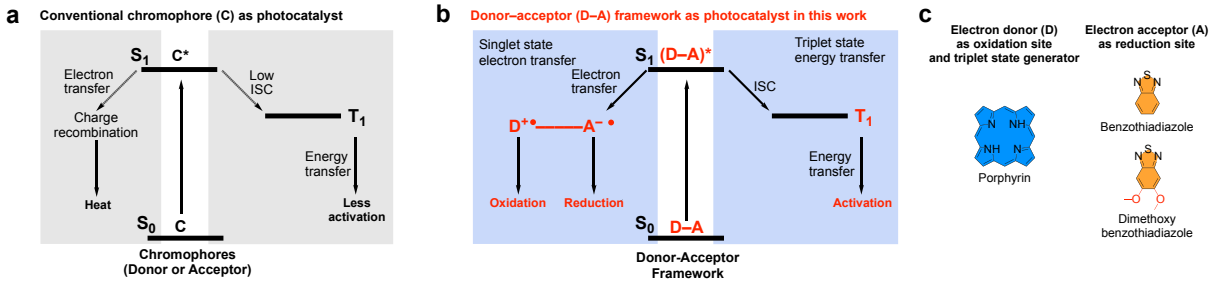

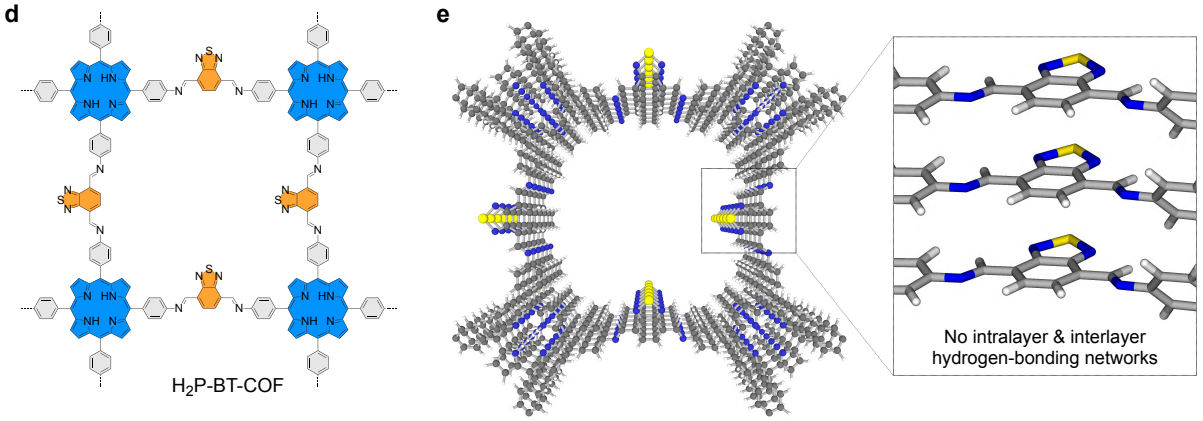

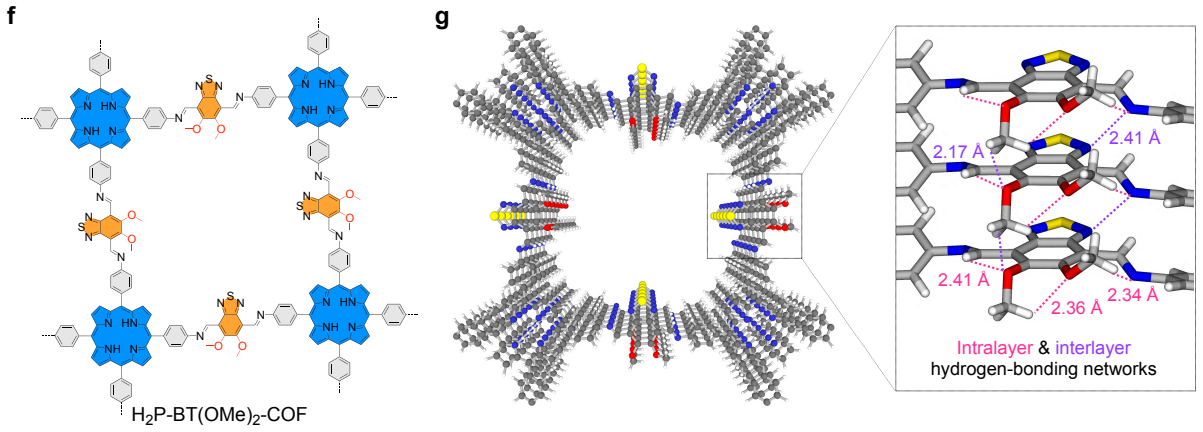

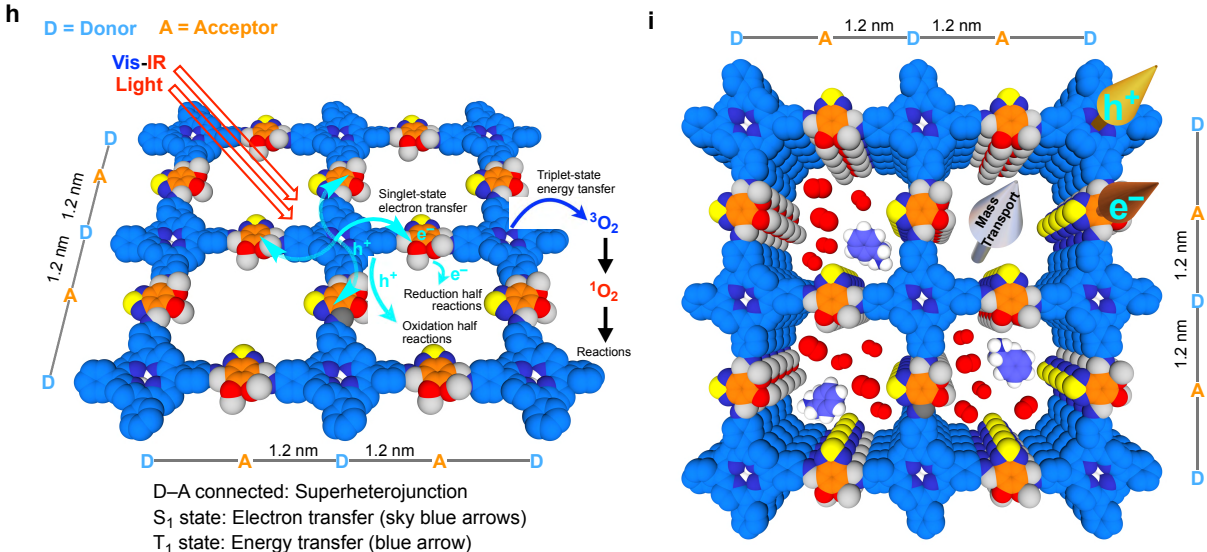

D–A connected: Superheterojunction
S_1 state: Electron transfer (sky blue arrows)
T_1 state: Energy transfer (blue arrow)

D–A skeletons: Light absorption and catalytic centres
π columns: Electron and hole supply chains
1D pores: Reactant/substrate transport and product release

Fig. 1 | Photoexcited states and donor-acceptor framework photocatalysts. a, Photoexcited states and catalytic pathways for conventional chromophore-based photocatalysts via either singlet (S_1) or triplet states (T_1). **b,** Photoexcited states and dual-channel catalysis from both S_1 and T_1 in the electron donor-acceptor framework photocatalyst. **c**, Structures of porphyrin as electron donor, T_1 generator and oxidation site, and benzothiadiazole/dimethoxy benzothiadiazole as acceptor and reduction site. **d, e,** Chemical (**d**) and reconstructed crystal structures (**e**) of H_2P-BT-COF (blue porphyrin: donor; orange benzothiadiazole: acceptor). Inset shows the absence of hydrogen bonds. **f, g,** Chemical (**f**) and reconstructed crystal structures (**g**) of H_2P-BT(OMe)$_2$-COF. Inset shows well-developed intralayer and interlayer hydrogen bonds. **h,** Reconstructed one layer structure of H_2P-BT(OMe)$_2$-COF. Each donor (D in blue) is connected to four acceptors (A in orange) and each acceptor is linked with two donors along the *x* and *y* directions at a regular interval of 1.2 nm. Sky blue arrows show photoinduced electron transfer at S_1 to form oxidized and reduced units which serve as oxidation and reduction centres to promote photocatalysis. Blue arrow shows energy transfer from T_1 to activate reactants and facilitate reactions. **i,** Reconstructed stacking layer structures (5 layers) shows the porphyrin donor columns for hole transport and benzothiadiazole acceptor columns for electron transport, while the aligned 1D pores offer highways for reactant and substrate supply and product release (only O_2 and benzylamine are shown).

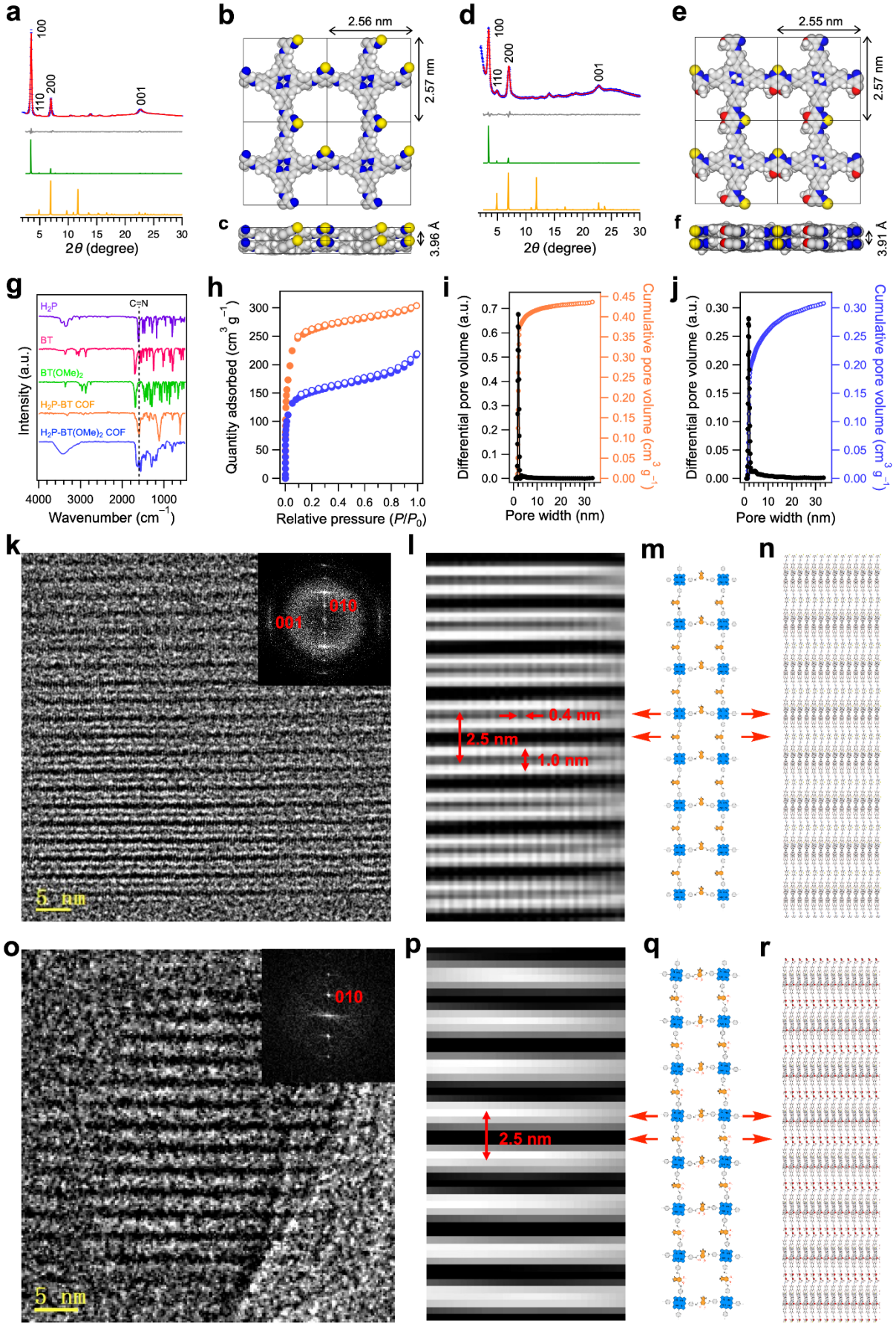
a
100
110
200
001
5 10 15 20 25 30
2θ (degree)
b
2.56 nm
2.57 nm
c
3.96 Å
d
100
110
200
001
5 10 15 20 25 30
2θ (degree)
e
2.55 nm
2.57 nm
f
3.91 Å
g
H2P
BT
BT(OMe)2
H2P-BT COF
H2P-BT(OMe)2 COF
C=N
Intensity (a.u.)
4000 3000 2000 1000
Wavenumber (cm−1)
h
Quantity adsorbed (cm3 g−1)
0 50 100 150 200 250 300
0.0 0.2 0.4 0.6 0.8 1.0
Relative pressure (P/P0)
i
Differential pore volume (a.u.)
0.0 0.1 0.2 0.3 0.4 0.5 0.6 0.7
Cumulative pore volume (cm3 g−1)
0.00 0.05 0.10 0.15 0.20 0.25 0.30 0.35 0.40 0.45
0 10 20 30
Pore width (nm)
j
Differential pore volume (a.u.)
0.00 0.05 0.10 0.15 0.20 0.25 0.30
Cumulative pore volume (cm3 g−1)
0.00 0.05 0.10 0.15 0.20 0.25 0.30
0 10 20 30
Pore width (nm)
k
001
010
5 nm
l
0.4 nm
2.5 nm
1.0 nm
m
n
o
010
5 nm
p
2.5 nm
q
r

Fig. 2 | Crystal and porous structures. a, d, PXRD patterns of experimentally obtained (blue cross), Pawley refinement (red curve), their differences (grey curve), simulated AA-stacking (green curve) and AB-stacking (orange curve) modes of H_2P-BT-COF (**a**) and H_2P-BT(OMe)$_2$-COF (**d**). **b, e,** Top views of unit cell of H_2P-BT-COF (**b**) and H_2P-BT(OMe)$_2$-COF (**e**). **c, f,** Side views of unit cell of H_2P-BT-COF (**c**) and H_2P-BT(OMe)$_2$-COF (**f**). **g,** FT IR spectra of the COFs and monomers. **h,** Nitrogen sorption isotherms of the COFs (filled dots: adsorption, open circles: desorption; orange: H_2P-BT-COF, blue: H_2P-BT(OMe)$_2$-COF). **i, j,** Cumulative pore volume (open circles) and pore size distribution (filled dots) of H_2P-BT-COF (**i**) and H_2P-BT(OMe)$_2$-COF (**j**). **k-n,** HR TEM image (**k**), FFT image (inset), IFFT image (**l**), one-pore lane structure (**m,** top view) and stacked layers (**n,** side view) of H_2P-BT-COF. **o-r,** HR TEM image (**o**), FFT image (inset), IFFT image (**p**) and one-pore lane structure (**q,** top view) and stacked layers (**r,** side view) of H_2P-BT(OMe)$_2$-COF. In **m** and **q**, red arrows suggest positions of molecular units.

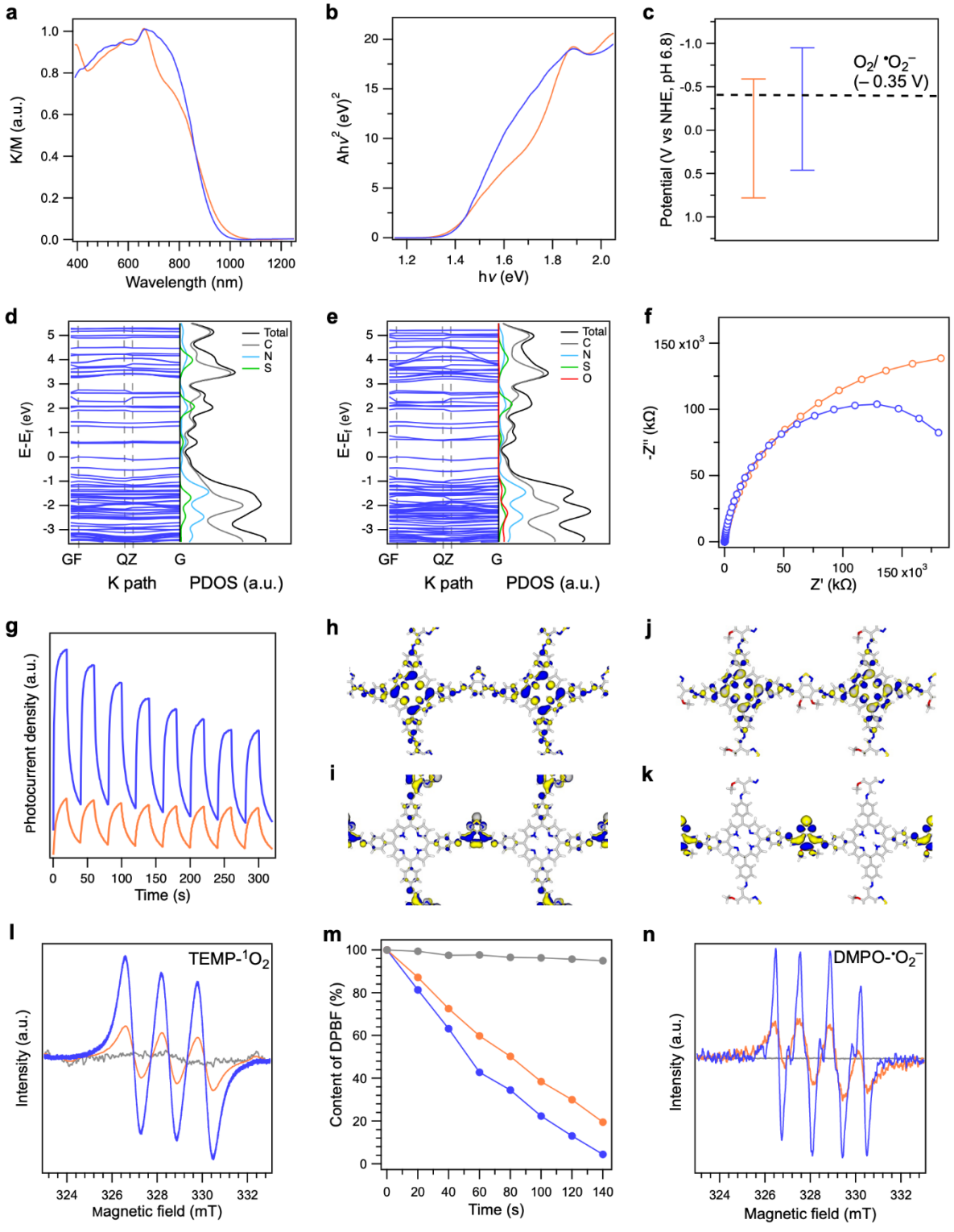

Fig. 3 | Photophysical properties and reaction intermediates. a, Solid-state electronic absorption spectra. **b,** Tauc plot. **c,** Experimentally derived energy levels of the D–A COFs compared to oxygen reduction (black dashed line at −0.35 V). **d, e,** Band structure and projected density of states for H_2P-BT-COF (**d**) and H_2P-BT$(OMe)_2$-COF (**e**). **f,**

Electrochemical impedance spectra. **g,** Photocurrent density. **h, i,** The highest occupied molecular orbital (HOMO, **h**) and the lowest unoccupied molecular orbital (LUMO, **i**) of H_2P-BT-COF. **j, k,** The HOMO (**j**) and LUMO (**k**) of H_2P-BT$(OMe)_2$-COF. **l,** Electron paramagnetic resonance (EPR) spectra of COFs in the dark (grey curve) and upon red light irradiation (λ = 620 nm) for 3 minutes in the presence of TEMP. **m,** Degradation of DPBF (40 μM) under air, in the presence of H_2P-BT$(OMe)_2$-COF (10 μg mL^{-1}, blue curve) dispersed in acetonitrile, under red light irradiation (λ = 620 nm), as compared to H_2P-BT-COF (orange curve) and without photocatalyst (grey curve). **n,** EPR spectra of COFs in the dark (grey curve) and upon red light irradiation (λ = 620 nm) for 3 minutes in the presence of DMPO. In **a** – **c**, **f**, **g** and **l** – **n**, orange colour: H_2P-BT-COF, blue colour: H_2P-BT$(OMe)_2$-COF.

a Oxidative coupling

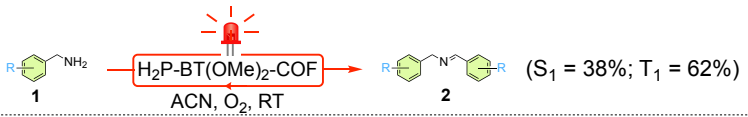

1

2

2a 10 min, 98% (99%) | **2b** 10 min, 98% (99%) | **2c** 10 min, 96% (99%) | **2d** 10 min, 95% (99%) | **2e** 10 min, 99% (99%) | **2f** 10 min, 99% (99%) | **2g** 10 min, 99% (99%)

2h 10 min, 96% (99%) | **2i** 10 min, 90% (99%) | **2j** 10 min, 83% (99%) | **2k** 10 min, 92% (99%) | **2l** 10 min, 99% (99%) | **2m** 15 min, 86% (99%) | **2n** 15 min, 76% (99%)

2o 15 min, 78% (99%) | **2p** 10 min, 99% (99%)

b Condensation reaction

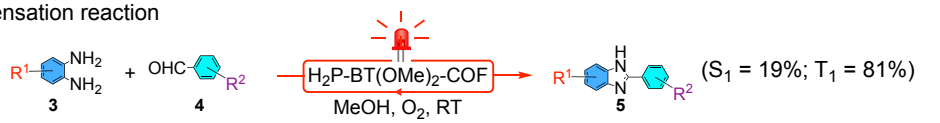

3 + 4

5

5a 1 h, 99% (93%) | **5b** 1 h, 99% (92%) | **5c** 1 h, 97% (90%) | **5d** 1 h, 98% (90%) | **5e** 1 h, 99% (91%) | **5f** 1 h, 99% (92%) | **5g** 1 h, 99% (90%)

5h 1 h, 99% (91%) | **5i** 1 h, 99% (89%) | **5j** 1 h, 94% (86%) | **5k** 1 h, 97% (88%) | **5l** 1 h, 99% (90%) | **5m** 1 h, 97% (89%) | **5n** 1 h, 99% (89%)

5o 1 h, 88% (82%) | **5p** 1 h, 85% (80%) | **5q** 1 h, 85% (79%) | **5r** 1 h, 95% (89%) | **5s** 1 h, 99% (92%) | **5t** 1 h, 88% (81%) | **5u** 1 h, 90% (84%)

5v 1 h, 94% (87%) | **5w** 1 h, 99% (92%) | **5x** 1 h, 99% (90%) | **5y** 1 h, 69% (64%) | **5z** 1 h, 90% (83%) | **5aa** 1 h, 90% (85%) | **5ab** 1.5 h, 96% (90%)

c C–C bond formation via C(sp^3)–H activation/cross-dehydrogenative coupling

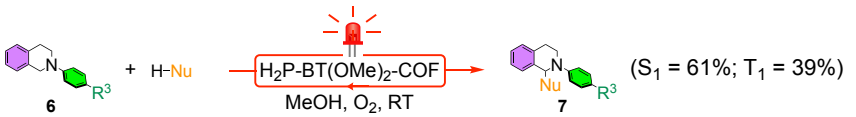

6 + H–Nu

7

7a 1.5 h, 98% (91%) | **7b** 1.5 h, 98% (89%) | **7c** 1.5 h, 98% (91%) | **7d** 1.5 h, 95% (88%) | **7e** 1.5 h, 96% (90%) | **7f** 1.5 h, 97% (91%) | **7g** 1.5 h, 96% (91%)

7h 2 h, 87% (83%) | **7i** 1.75 h, 88% (83%) | **7j** 1.75 h, 88% (82%) | **7k** 2 h, 94% (89%) | **7l** 2 h, 58% (53%) | **7m** 2 h, 77% (71%) | **7n** 1.5 h, 96% (89%)

7o 1.5 h, 95% (87%) | **7p** 1.5 h, 91% (85%) | **7q** 1.5 h, 97% (90%) | **7r** 1.5 h, 90% (83%) | **7s** 1.5 h, 95% (86%) | **7t** 1.5 h, 98% (90%) | **7u** 1.5 h, 96% (88%)

7v 2 h, 83% (79%) | **7w** 1.5 h, 95% (87%) | **7x** 1.75 h, 93% (86%) | **7y** 1.5 h, 93% (84%) | **7z** 1.5 h, 89% (82%) | **7aa** 2 h, 91% (84%) | **7ab** 1.75 h, 93% (85%)

Fig. 4 | Coupling and condensation reactions by photocatalytic H_2P-BT(OMe)$_2$-COF. a, Oxidative coupling reactions (yield determined by GC-MS, numbers in parenthesis represent selectivity) upon irradiation with 620-nm red light LED. **b,** Condensation reactions (yield determined by ^{1}H NMR, numbers in parenthesis represent isolated yield) upon irradiation with 620-nm red light LED. **c,** C–C bond formation via C(sp^3)–H activation/cross-dehydrogenative coupling upon irradiation with 620-nm red light LED (yield determined by ^{1}H NMR, numbers in parenthesis represent isolated yield). In **a**–**c**, Values in paratheses right to the reaction schemes show the contribution of S_1 and T_1 to the reactions.

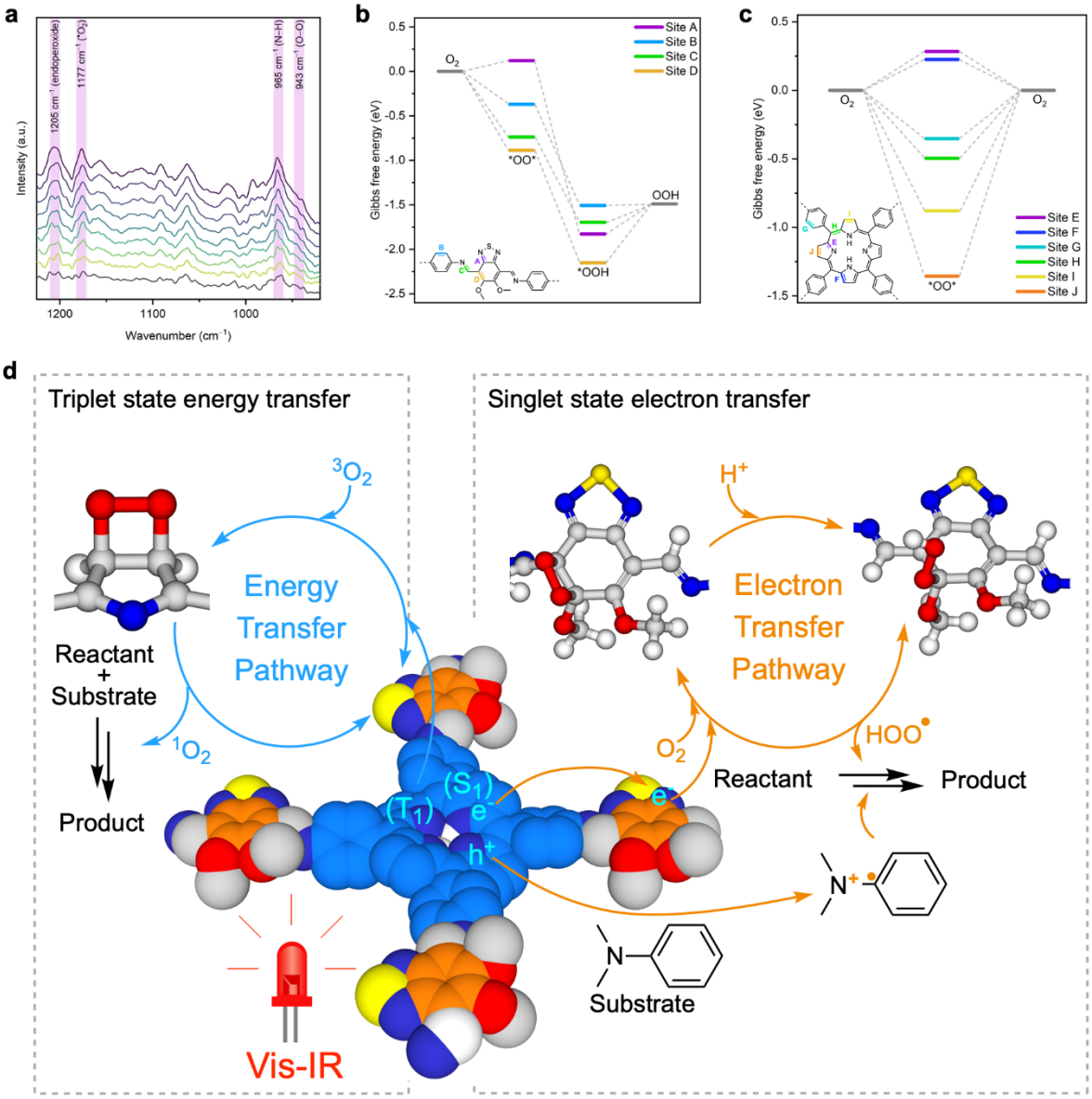

Fig. 5 | Photocatalytic sites and reaction mechanism. a, In situ DRIFTS of H_2P-BT$(OMe)_2$-COF under O_2. **b, c,** Gibbs free energy diagrams for electron transfer (**b**) and energy transfer (**c**) to oxygen over H_2P-BT$(OMe)_2$-COF. **d,** Dual pathway activation mechanism of both energy transfer via T_1 and electron transfer through S_1 in H_2P-BT$(OMe)_2$-COF, without the need of cocatalysts and sacrificial agents.

Methods

Chemicals

All starting materials and chemicals used in the experiments were purchased from Merck, Tokyo Chemical Industry and Sigma-Aldrich or GCE Laboratory chemicals and used without prior purification. Ethyl acetate (EA), methanol (MeOH), ethanol (EtOH), *N,N*-dimethylformamide (DMF), acetone and acetic acid (AcOH) were obtained from VWR Chemical. Dichloromethane (DCM), hexanes and chloroform were obtained from Fisher Scientific. Tetrahydrofuran (THF) was obtained from ACI Labscan. *n*-Propanol (*n*-PrOH), trifluoromethanesulfonic acid (TfOH), 1,2-dichlorobenzene (*o*-DCB) and mesitylene were obtained from Tokyo Chemical Industry. Dioxane and *n*-butanol (*n*-BuOH) were obtained from Sigma-Aldrich. Diethyl ether (Et_2O) and acetonitrile (ACN) were obtained from Avantor Performance Materials.

Powder X-ray diffraction (PXRD)

PXRD measurements were performed on a Bruker D8 Focus model Powder X-ray Diffractometer using Cu/K_α radiation (40 kV, 40 mA) at room temperature by depositing powder on PMMA specimen holder, from $2\theta = 2°$ to 30° with 0.02° increment.

Single crystal X-ray diffraction (XRD)

XRD measurements were performed on a Bruker Venture D8 diffractometer. The crystal was kept at 100.00 K during data collection. Using Olex2, the structure was solved with the SHELXT structure solution program using Intrinsic Phasing and refined with the SHELXL refinement package using Least Squares minimisation.

Nitrogen sorption

Nitrogen sorption isotherms were measured at 77 K with a Micromeritics Instrument Corporation model 3Flex surface characterisation analyser. The Brunauer–Emmett–Teller (BET) method was utilised to calculate the specific surface areas. By using the quenched solid density functional theory model, the pore volume and pore sizes were derived from the sorption curve.

Acetonitrile sorption

Acetonitrile sorption isotherms were measured at 298 K with a BELSORP MAX X instrument. The Brunauer–Emmett–Teller (BET) method was utilised to calculate the quantity adsorbed.

Fourier-transform infrared (FT IR) spectroscopy

FT IR spectra were recorded on a Bruker model VERTEX 80v spectrometer using KBr pellets.

Thermogravimetric analysis (TGA)

TGA data was collected using a TA Instruments Q500 by heating from 40 to 800 °C at a rate of 10 °C min^{-1} under nitrogen flow (10 mL min^{-1}).

Solution-state NMR spectroscopy

^{1}H and ^{13}C NMR spectra were acquired on a Bruker AVANCE I 500 MHz NMR spectrometer.

Solid-state NMR spectroscopy

Solid-state ^{13}C cross polarisation magic angle spinning (CP/MAS) NMR spectra were measured on AVNEO400 solid NMR spectrometer.

Electron paramagnetic resonance (EPR) spectroscopy

EPR data were obtained by a JEOL model JES-FA200 EPR spectrometer by using 5,5-dimethyl-1-pyrroline *N*-oxide (DMPO) (0.1 M) and 2,2,6,6-tetra-methyl-1-piperidine (TEMP) (0.1 M) as the spin trap, which forms an adduct with the $^{\bullet}O_2^-$ and $^1O_2$ produced respectively

837 during photoirradiation (30-W red light LED, λ = 620 nm) in the presence of photocatalysts.
838 The data were collected on the measurement parameters, scanning frequency: 9050 MHz;
839 scanning power, 5 mW; central field, 323 mT; scanning width, 100 G; scanning temperature:
840 298 K.

841 **Electronic absorption spectroscopy**

842 Electronic absorption spectroscopy was conducted on a JASCO model V-570
843 spectrophotometer.

844 **Field emission scanning electron microscopy (FE SEM)**

845 FE SEM images were taken on a JEOL model JSM-6701F operating at an accelerating voltage
846 of 5.0 kV. The samples were prepared by drop-casting isopropanol suspension onto silica wafer
847 and coated with gold.

848 **High resolution transmission electron microscopy (HR TEM)**

849 The COF samples were dispersed in tetrahydrofuran suspension and then drop-casted onto a
850 200-mesh copper grid covered with a layer of carbon film. Visualization of crystalline COF
851 structures was conducted on the Thermo Scientific Spectra 300 TEM (Thermo Fisher Scientific)
852 operating at an accelerating voltage of 300 kV. Equipped with an image corrector and a K3
853 camera, all images were recorded under a low dose mode to minimize the damage of electron
854 beam to the crystal structures. For H_2P-BT-COF, totally 100 frames were taken during
855 exposure of 10 seconds, using counting and CDS mode of K3 camera. The drift correction,
856 alignment and superposition of 100 images were carried out on Digital Micrography software
857 (Gatan). The electron density was 1.5 $e^- A^{-2} s^{-1}$, and the total electron dose of the accumulated
858 drift-corrected image is 15.2 $e^- A^{-2}$. For H_2P-BT(OMe)$_2$-COF, totally 150 frames were taken
859 during exposure of 15 seconds, using counting and CDS mode of K3 camera. The drift

correction, alignment and superposition of 150 images were carried out on Digital Micrography software (Gatan). The electron density was 2.33 $e^{-} A^{-2} s^{-1}s$, and the total electron dose of the accumulated drift-corrected image is 35.1 $e^{-} A^{-2}$.

Transient absorption spectroscopy (TA)

Nanosecond transient absorption measurements were conducted using the ultrafast pump pulses along with an electronically delayed supercontinuum light source with a sub-nanosecond pulse duration (EOS, Ultrafast Systems, Sarasota, FL, USA).

Fluorescence spectroscopy

The fluorescence spectra were measured on a JASCO model FP-6600 spectrofluorometer. The COF samples were dispersed in acetonitrile and excited at λ = 420 nm.

Time-resolved fluorescence spectroscopy

The decay curves were measured on a Hamamatsu model compact fluorescence lifetime spectrometer C11367 (Quantaurus-Tau) that contains a light-emitting diode (LED) pulsed light source, monochromator, PMT (photomultiplier tube), iris (aperture) for adjusting light level and filter for cutting excitation light. The COF samples were dispersed in acetonitrile and irradiated with internal LED at λ = 405 nm. The decay curves were fitted to a double exponential function of the form: $\tau_{avg} = A_1 e^{-t/\tau_1} + A_2 e^{-t/\tau_2}$.

Phosphorescence spectroscopy

Phosphorescence spectra were recorded with an Edinburgh model FLS1000 spectrofluorometer equipped with a Hamamatsu NIR photomultiplier detector (C9940-02), in conjunction with either a continuous-wave 808 nm (MDL-III-808 nm) or 980 nm diode laser (MDL-III-980 nm).

Elemental analysis

Elemental analysis was tested with a ThermoFisher Scientific FlashSmart CHNS Elemental Analyzer by weighing the samples in tin containers and then combusted at high temperature with oxygen.

In situ diffuse reflectance infrared Fourier transform spectroscopy (DRIFTS)

DRIFTS measurements were performed on a Nicolet iS50 FT-IR. The photocatalyst was filled into an in-situ IR holder in the chamber. Before the measurement, the chamber was degassed under argon flow at a rate of 20 ml min^{-1} for 1 hour. The baseline was then obtained at room temperature. Then, oxygen and water vapour were purged into the chamber for 1 hour under dark condition. Irradiation under visible light through the window of the chamber was initiated and the spectra were recorded at specific intervals.

Photoelectrochemical measurements

Electrochemical impedance, Mott-Schottky and photocurrent measurements were recorded on Electrochemical Analyzer model 610B using a typical three-electrode system consisting of COF-coated FTO working electrode, Pt wire counter electrode and Ag/AgCl reference electrode. Degassed Na_2SO_4 solution (0.2 M, pH = 6.8) was used as the electrolyte for all measurements. A 620 nm red-light LED (30 W) was used for the photocurrent measurements.

The COF-coated FTO working electrode was prepared by spreading finely dispersed (by sonication) COF (1 mg) in *N*,*N*-dimethylformamide (0.5 mL) solution containing 5 wt% Nafion (0.1 mL) onto a 1 cm × 1 cm FTO plate, followed by drying in a 70 °C oven for 60 minutes.

The potentials against Ag/AgC*l* were converted to NHE potentials using the equation:

$E_{NHE} = E_{Ag/AgCl} + E^0_{Ag/AgCl}$ ($E^0_{Ag/AgCl} = 0.199$ V)

Gas chromatography-Mass spectrometry (GC-MS)

GC analyses were performed on an Agilent GC-7890B gas chromatograph with an FID detector using a DB-5MS column (30 m, 0.25 mm). GC-MS analyses were performed on a Shimadzu model QP2010 SE using a DB-5MS column (30 m, 0.25 mm I.D.).

Flash-photolysis time resolved microwave conductivity (FP-TRMC) measurements

FP-TRMC measurements of the COFs prepared and fixed over quartz substrate using PMMA/toluene and non-conducting tape. The transient electronic conductivity was evaluated under N_2 and SF_6 atmosphere and by immersing Et_3N on the quartz substrates, respectively. The probing microwave was led into a transverse electric (TE) mode microwave cavity with the Q-value of 2000, leading to $\tau = Q/2f \sim 100$ ns and the microwave frequency and power were set at around 9.1 GHz and 3.5 mW, respectively. Transient charge carries were generated through photoinduced charge separation by using a third harmonic generation (λ = 355 nm) from a Spectra Physics INDI-HG Nd:YAG laser with a pulse duration of 5-8 ns. The photon density was 9.11×10^{15} cm^{-2} for the 355-nm laser pulse (10 mW) and 5.32×10^{15} cm^{-2} for the 266-nm laser pulse (5 mW). The photoconductivity transient demodulated through a GaAs crystal-diode with Schottky-barriers (rise time <1 ns) and monitored by a Tektronix model TDS3034B digital oscilloscope. The observed conductivities were normalised, given by a photocarrier generation yield (Φ) multiplied by sum of the carrier mobilities of electron/hole ($\Sigma\mu$), according to the equation,

$$\Phi\Sigma\mu = A\Delta P_R / eI_0F_LP_R$$

where, e, A, I_0, F_L, P_R and ΔP_R are elementary charge, sensitivity factor (S cm^{-1}), incident photon density of the excitation laser (photon cm^{-2}), correction factor (cm^{-1}) for overlapping between special distribution of photo-generated charge carriers and electromagnetic field strength of probing microwave in the cavity and reflected microwave power and its transient change, respectively.

Photocatalytic DPBF quenching

An air-saturated acetonitrile solution (100 mL) was added COF photocatalyst (1 mg). The solution was sonicated for 5 minutes before the addition of 1,3-diphenylisobenzofuran (DPBF) to reach a concentration of 40 μM. The solution was then irradiated with 620 nm red-light LED (30 W) with constant coil fan cooling.

A 1-mL aliquot was withdrawn every 20 seconds, followed by centrifugation and filtration through 0.22 μm PTFE filter to remove the photocatalyst. The concentration of DPBF remaining in the solution was determined from UV-vis absorbance at 418 nm.

Photocatalytic oxidative couplings

An air-saturated acetonitrile solution (10 mL) was added COF photocatalyst (2 mg, 0.45 mol%). The solution was sonicated for 5 minutes before the addition of benzylamine (0.4 mmol). The solution was then irradiated with 620-nm red light LED (30 W) with constant coil fan cooling.

After completion of the reaction, the mixture was centrifuged and filtered through 0.22 μm PTFE filter to remove the photocatalyst. The filtrate was analysed using gas chromatography–mass spectrometry with FID detector.

For recycling experiments, an air-saturated acetonitrile solution (100 mL) was added COF photocatalyst (25 mg). The solution was sonicated for 5 minutes before the addition of benzylamine (0.4 mmol). The solution was then irradiated with 620 nm red-light LED (30 W) with constant coil fan cooling. After completion of the reaction, the suspension was filtered, and the filtrate was analysed using gas chromatography–mass spectrometry with FID detector. H_2P-BT(OMe)$_2$-COF was then washed with acetonitrile and dried under vacuum at 120 °C for 1 hour before reuse.

Photocatalytic condensation reactions

An oxygen-saturated methanol solution (4 mL) was added COF photocatalyst (2 mg). The solution was sonicated for 5 minutes before the addition of 1,2-diaminobenzene (0.15 mmol) and benzaldehyde (0.1 mmol). The solution was then irradiated with 620 nm red-light LED (30 W) with constant coil fan cooling.

After completion of the reaction, the mixture was centrifuged and filtered through 0.22 μm PTFE filter to remove the photocatalyst. The solvent was removed by vacuum evaporation and 1,3,5-trimethoxybenzene was added as an internal standard for conversion analysis using ^{1}H NMR spectroscopy. Afterwards, the reaction was subjected to column chromatography (hexane/ethyl acetate = 3/1 v/v) to obtain the purified products.

For recycling experiments, an oxygen-saturated methanol solution (15 mL) was added COF photocatalyst (25 mg). The solution was sonicated for 5 minutes before the addition of 1,2-diaminobenzene (0.15 mmol) and benzaldehyde (0.1 mmol). The solution was then irradiated with 620-nm red light LED (30 W) with constant coil fan cooling. After completion of the reaction, the suspension was filtered and the filtrate was analysed using ^{1}H NMR spectroscopy, with 1,3,5-trimethoxybenzene as the internal standard. H_2P-BT(OMe)$_2$-COF was then washed with methanol and dried under vacuum at 120 °C for 1 hour before reuse.

Photocatalytic C–C bond formations

An oxygen-saturated methanol solution (5 mL) was added COF photocatalyst (2 mg). The solution was sonicated for 5 minutes before the addition of 2-phenyl-1,2,3,4-tetrahydroisoquinoline (0.1 mmol) and the corresponding nucleophile (0.3 mmol). When acetone is used as a nucleophile, acetone (10 mmol) and *L*-proline (0.03 mmol) were added. The solution was then irradiated with 620-nm red light LED (30 W) with constant coil fan cooling.

After completion of the reaction, the mixture was centrifuged and filtered through 0.22 μm PTFE filter to remove the photocatalyst. The solvent was removed by vacuum evaporation and 1,3,5-trimethoxybenzene was added as an internal standard for conversion analysis using ^{1}H NMR spectroscopy. Afterwards, the reaction was subjected to column chromatography (hexane/ethyl acetate = 20/1 v/v) to obtain the purified products.

For recycling experiments, an oxygen-saturated methanol solution (20 mL) was added COF photocatalyst (25 mg). The solution was sonicated for 5 minutes before the addition of 2-phenyl-1,2,3,4-tetrahydroisoquinoline (0.1 mmol) and nitromethane (0.3 mmol). The solution was then irradiated with 620-nm red light LED (30 W) with constant coil fan cooling. After completion of the reaction, the suspension was filtered and the filtrate was analysed using ^{1}H NMR spectroscopy, with 1,3,5-trimethoxybenzene as the internal standard. H_2P-BT(OMe)$_2$-COF was then washed with methanol and dried under vacuum at 120 °C for 1 hour before reuse.

Computational studies

Molecular modelling and Pawley refinement[32] were carried out using Reflex, a software package for crystal determination from PXRD pattern, implemented in Materials Studio 2020 (Accelrys Inc.). We performed Pawley refinement to optimise the lattice parameters iteratively until the R_{wp} and R_p values converge. The Thompson-Cox-Hastings profile function[84] for whole profile fitting and asymmetry correction function as Berar-Baldinozzi[85] were used during the refinement processes.

The crystalline structures of COFs were determined using the density-functional tight-binding (DFTB+) method including Lennard-Jones (LJ) dispersion[86, 87]. DFTB+ is an approximate density functional theory method based on the empirical tight-binding approach, utilising an optimised minimal LCAO Slater-type all-valence basis set in combination with a two-centre approximation for Hamiltonian matrix elements. The lattice dimensions were optimised

simultaneously with the geometry. Standard DFTB parameters for X–Y element pair (X, Y = C, H, N, O, S) interactions were employed from the *mio* set[88].

Optical and electronic calculations were performed using CASTEP, a software package using density functional theory (DFT) as a basis. Starting with the COF structures, we performed DFT calculations using the generalised gradient approximation (GGA) method and Perdew-Burke-Ernzerhof (PBE) exchange-correlation functional[89]. During structural optimisation, a cutoff energy of 400 eV was employed for the plane-wave basis set, with 0.01 eV $Å^{-1}$ as the force and 5×10^{-6} eV as the energy convergence tolerance, with *k*-point set of $1 \times 1 \times 8$.

Hydrogen bonding calculations were performed using the built-in hydrogen bond calculation dialog based on density functional theory (DFT), on the optimised COF structures. Hydrogen bonding scheme was enabled for N, O, S, halogens and C as hydrogen-bond donors, while the maximum hydrogen-bond acceptor distance (2.5 Å) and minimum donor-hydrogen-acceptor angle (90°) was set at default values[90].

The reduction of O_2 to superoxide radical anion is initiated by the adsorption of O_2 on active sites of COFs. Since the superoxide radical anion generated is consumed in various organic transformations subsequently, we modelled the Gibbs free energy for *OOH formation as a method for indirect comparison. The reaction process for the formation of *OOH has been well studied and has been shown to involve the following steps[91–93]:

$$* + O_2 \rightarrow *OO* \quad (1)$$

$$*OO* + H^+ + e^- \rightarrow *OOH \quad (2)$$

$$*OOH \rightarrow * + {}^\bullet OOH \quad (3)$$

H_2P-BT(OMe)$_2$-COF was modelled using a monolayer structure sandwiched between 25 Å vacuum slab to avoid dipole effects. Due to the predominant localisation of photogenerated

electron on the benzothiadiazole unit, possible active sites on the benzothiadiazole unit were explored. During all optimisations, a cutoff energy of 400 eV was employed for the plane-wave basis set, with 0.01 eV $Å^{-1}$ as the force and 5×10^{-6} eV as the energy convergence tolerance.

Charge analysis was performed using geometrically optimised COFs, at GGA-PBE level. The *k*-point set was at $1 \times 1 \times 4$ and all electrons were considered in core treatment, using the DNP basis set[94].

Acetonitrile and O_2 adsorption calculations were performed using geometrically optimised COFs, at pressure of 101 kPa and temperature of 298 K. The methodology employs Metropolis Monte Carlo (MC) method, which treats sorbate molecules as rigid entities, focusing on their translational and rotational movements within the pore structure[95].

Acknowledgements D.J. acknowledges Singapore MOE Tier 2 grant (T2EP10221-0012) and Singapore NRF A*STAR grant (U2102d2004). N.Y. thanks the NRF Investigatorship (NRFI07–2021–0015) for financial supports. J.L. acknowledges financial support from the National Natural Science Foundation of China (52273208), the Natural Science Foundation of Shanxi Province (202203021211289) and the Research Project supported by Shanxi Scholarship Council of China (2022-004). We acknowledge Y.G and X.L. (NUS) for oxygen phosphorescence spectroscopy.

Author contributions D.J. conceived the concept and led the project. R.L., D.Z. and Y.C. conducted the experiments and measurements. M.F. and T.C.S. conducted and analysed the transient absorption measurements. T.W. and N.Y. conducted the in situ diffuse reflectance infrared Fourier transform spectroscopy measurements. H.S. and M.L. conducted the high-resolution transmission electron microscopy measurements. J.L. conducted nitrogen and acetonitrile sorption measurements. S.J. and S.S. conducted flash-photolysis time-resolved microwave conductivity measurements. R.L., D.Z., J.S., H.S., Y.C., M.F., T.W., J.L., M.L.,

T.C.S., N.Y., S.S. and D.J. interpreted the results and R.L., D.Z. and D.J. wrote the manuscript. All authors have read and commented on the manuscript.

Competing interests The authors declare no conflict of interest.

Additional information

Supplementary information The online version contains supplementary material available at XXX.

Correspondence and requests for materials should be addressed to Donglin Jiang

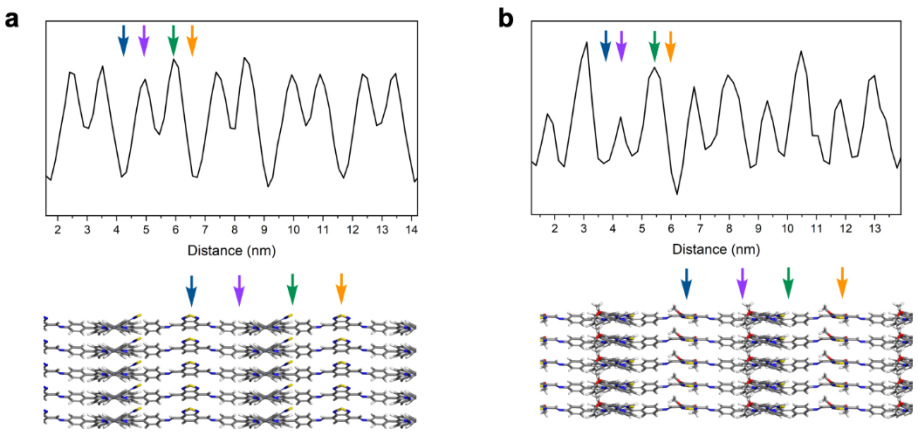

Extended Data Fig. 1 | HR TEM live profile. a, b, HR TEM live profile of H_2P-BT-COF (**a**) and H_2P-BT(OMe)$_2$-COF (**b**). In the HR TEM live profile of H_2P-BT-COF, distances of 4.97 nm and 5.93 nm come from the left side and right side of the porphyrin unit, respectively (**a**, purple and green arrows), while the benzimidazole unit show distances at 4.16 nm and 6.73 nm (**a**, blue and orange arrows). Similarly, in H_2P-BT(OMe)$_2$-COF, the porphyrin unit exhibits the highest peaks of 4.27 nm and 5.43 nm (**b**, purple and green arrows), while the 2-methoxy-benzothiadiazole unit shows the lowest peaks of 3.68 nm and 6.2 nm, respectively (**b**, blue and orange arrows). HR TEM live profiles of both COFs revealed a lower peak between two high peaks, which comes from pore of porphyrin unit. The depth of the troughs suggests discrete spacing between atomic planes, consistent with the porous nature of the COFs.

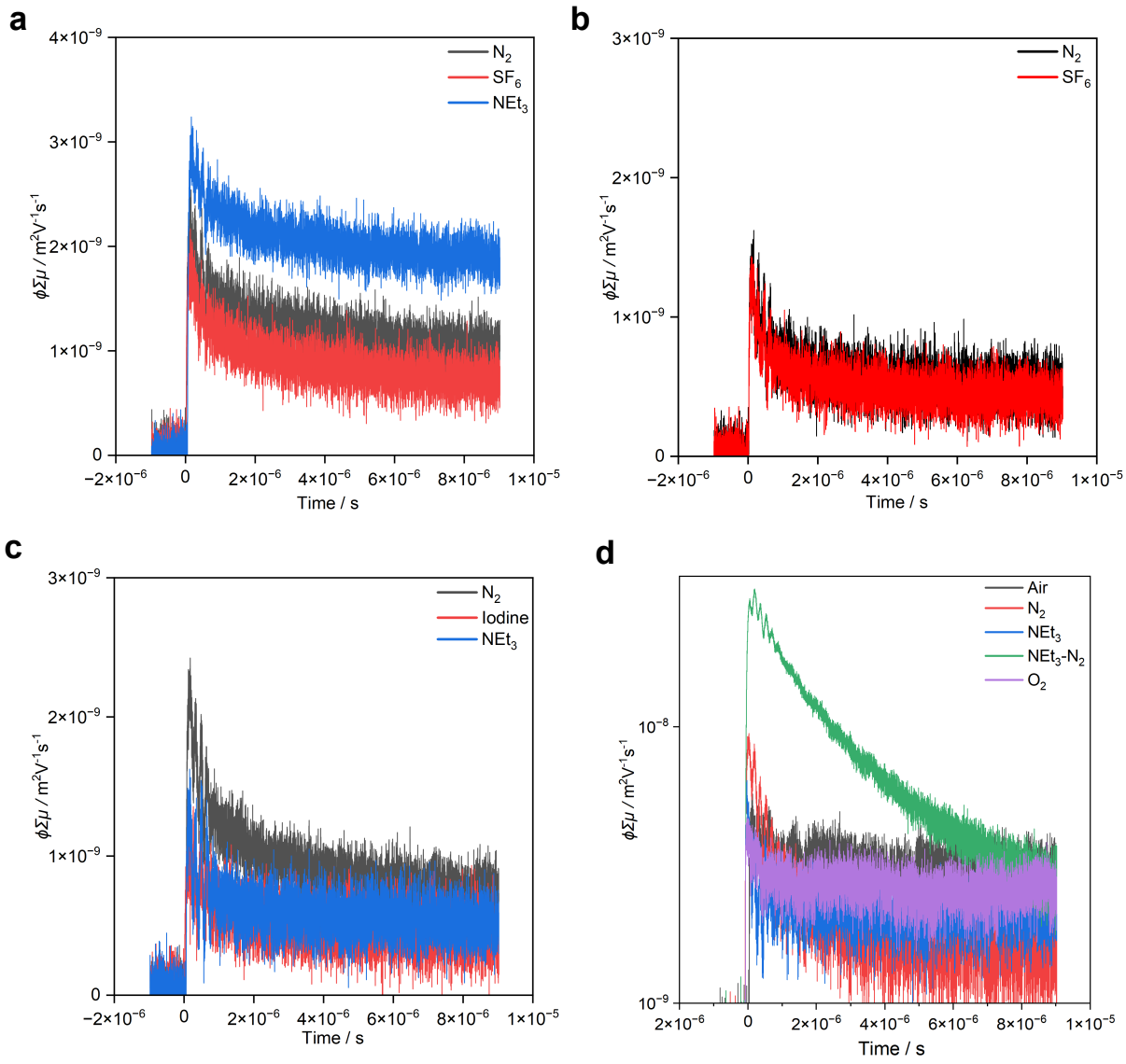

1064

1065 **Extended Data Fig. 2 | Flash-photolysis time resolved microwave conductivity (FP-**
1066 **TRMC) measurements. a,** FP-TRMC transients of H_2P-BT-COF under N_2 (black), SF_6 (red)
1067 and Et_3N (blue) atmosphere upon excitation at 355 nm. **b,** FP-TRMC transients of H_2P-
1068 BT$(OMe)_2$-COF under N_2 (black) and SF_6 (red) upon excitation at 355 nm. **c,** FP-TRMC
1069 transients of H_2P-BT$(OMe)_2$-COF under N_2 (black), iodine (red) and Et_3N (blue) atmosphere
1070 upon excitation at 355 nm. **d,** Kinetics traces of H_2P-BT$(OMe)_2$-COF upon excitation at 266
1071 nm under N_2 (red), air (black), NEt_3 (blue), NEt_3 + N_2 (green) and O_2 (purple) atmosphere.

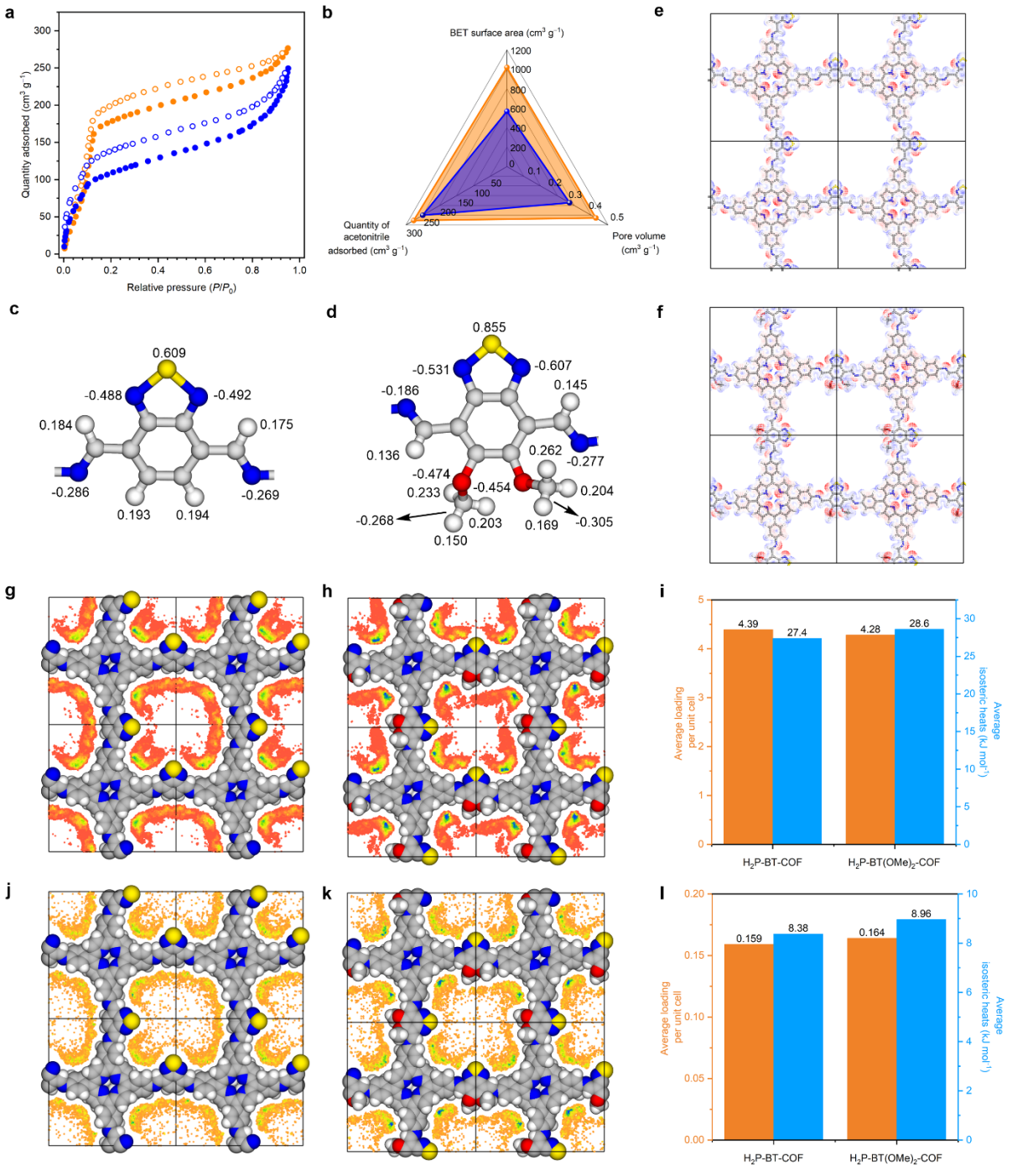

Extended Data Fig. 3 | Adsorption features. a, Acetonitrile sorption isotherms of the COFs (dots: adsorption, circles: desorption; orange: H_2P-BT-COF, blue: H_2P-BT(OMe)$_2$-COF). **b,** Radar plot for adsorption comparison of BET surface area, quantity of acetonitrile adsorbed and pore volume between H_2P-BT-COF (orange) and H_2P-BT(OMe)$_2$-COF (blue). **c, d,** Charge analysis of benzothidiazole units of H_2P-BT-COF (**c**) and H_2P-BT(OMe)$_2$-COF (**d**). **e, f,** Electrostatic potential map of H_2P-BT-COF (**e**) and H_2P-BT(OMe)$_2$-COF (**f**) (Red region =

negative charge, blue region = positive charge). **g, h,** Calculated acetonitrile density distribution of H_2P-BT-COF (**g**) and H_2P-BT(OMe)$_2$-COF (**h**) (Red region = low density, blue region = high density). **i, l,** Calculated average loading of adsorbate per unit cell and average isosteric heats for acetonitrile adsorption (**i**) and O_2 adsorption (**l**) at 101 kPa. **j, k,** Calculated oxygen density distribution of H_2P-BT-COF (**j**) and H_2P-BT(OMe)$_2$-COF (**k**) (Orange region = low density, blue region = high density).